Hydraulic fracturing for improved nutrient delivery in microbially-enhanced coalbed-methane (MECBM) production

Sheng Zhi[a,*], Derek Elsworth[a], Jiehao Wang[a], Quan Gan[b], Shimin Liu[a]

[a] Department of Energy and Mineral Engineering, EMS Energy Institute and G^3, Center, Pennsylvania State University, University Park, PA, 16802, USA
[b] Department of Petroleum Geology and Geology, School of Geosciences, University of Aberdeen, Aberdeen, Scotland, UK

ABSTRACT

Microbially enhanced coalbed methane (MECBM) recovery is a novel method to increase gas production by injecting nutrients, either with/without microorganisms, in depleted CBM wells. However, to be effective, methanogens require that the nutrient must be delivered efficiently by aqueous solution to a maximally large reservoir volume for microbial colonization. This study seeks to improve understanding of solute transport and microbial gas generation in naturally fractured reservoirs that are both pristine and hydraulically fractured. We complete a field-scale numerical simulation using an equivalent multi-continuum method to define the effectiveness of nutrient delivery. The complex pre-existing fracture pattern in the coalbed is represented by an overprinted discrete fracture network (DFN) to capture the natural heterogeneity and anisotropy of fracture permeability. A simplified PKN model is adopted to simulate hydraulic fracture propagation based on linear elastic fracture mechanics (LEFM). The hydraulically stimulated case is compared to the untreated control case, both without and with a network of natural fractures. Saturated cleat area, cumulative injection volume and prediction of methane yields are systematically modeled and analyzed for all three cases. We show that hydraulically stimulated fracture pathways, especially when connecting with a natural fracture network, optimally deliver nutrient remotely from the injection well, thereby increasing nutrient delivery and improving methane production and potential recovery. However, large magnitudes of proppant embedment and related permeability loss in the hydraulic fractures may reduce MECBM recovery. In the optimal production scenario, the methane production rate may reach 31 ft^3/ton, an approximately 5-fold increase over that from the pristine unstimulated case.

1. Introduction

Coalbed methane (CBM), defined as gas vented from gassy coal seams, contributes to a widespread unconventional natural gas resource. A rapid expansion of CBM development has occurred over the past two-decades in the United States, primarily in the San Juan, Powder River, Illinois, and Black Warrior basins (Ritter et al., 2015). It has been suggested that origin of CBM is either geological (i.e. thermogenic) at low temperatures or biological (i.e. methanogenic) at higher temperatures (Park and Liang, 2016; Stolper et al., 2014). Recent field- and laboratory-scale observations have identified that active and ongoing methanogenesis pervades some sedimentary basins, such as the Powder River Basin (Cokar et al., 2013; Kirk et al., 2012; Ulrich and Bower, 2008). In those basins, even coals that are insufficiently mature to have begun generating thermogenic gas appear to be methane rich. The abundance of methane in low- and intermediate-

maturity coals triggered geochemical studies on microbially enhanced CBM exploration (Strąpoć et al., 2011). If CBM can be microbially stimulated, the productive lifespans of depleted CBM wells can be extended, including generating microbial methane from areas without a prior history of gas production. Moreover, the microbially enhanced coalbed methane is an alternative method of utilizing existing coal resources, which entail restrictions on recovery due to the release of greenhouse gas and toxic emissions, i.e. sulfoxides and nitroxides, from conventional combustion of coal.

Understanding and improving the microbial process of bio-gasification is the key to enhance biogenic methane production from coal *in situ*. The biological process of microbial methanogenesis in coal has been hypothesized to begin with the solution of organic intermediates from the coal geopolymer. These soluble organics are then be biodegraded by microorganisms into substrates that are utilized by the anaerobic methanogens to produce CH_4 and CO_2 (Jones et al., 2010).

Studies have stimulated this natural bioconversion process by introducing manufactured nutrient solutions, consisting mostly of metal ions, yeast extract, peptone and methanol. Such bioconversion experiments at laboratory scale have shown that under optimal conditions, the biogenetic methane yield and content after 55 days are potentially 2900 ft^3/ton and 70% from powdered Illinois bituminous coal (Zhang et al., 2015, 2016a). The maximum yield from treated powdered coal from the San Juan Basin reaches 1041 ft^3/ton after 30 days using a formation water-based recipe (Bi et al., 2017). Although the coal granules provide a many-fold larger surface area for microbes to colonize than the unaltered coal matrix *in situ*, the promising productivity from bio-gasification suggests the significant potential of MECBM.

Field-scale tests have also been completed in commercial wells in the Powder River and Uinta Basins to generate additional bio-gas in areas where microbial CBM production has already been present. Currently, the proposed MECBM technique is to inject nutrient, either with or without methanobacterials, into coal seams to reactivate and accelerate the growth of coal-dependent methanogenesis and to increase bioavailability of coal organics. However, methanogenesis is presumed to mostly occur inside permeable fractures and macro-pores. The meso-/micro-pores in the coal matrix are typically too small for microorganisms (Scott, 1999; Zou et al., 2013). Meanwhile, the reservoir permeability of many coal fields, such as in Illinois, is < 1 mD. Extensive research has indicated that permeability is the most important factor in CBM production (Moore, 2012; Palmer, 2010; Wang et al., 2012, 2013; Wu et al., 2011). Delivery of the essential amendments into deep coal seams is limited if the reservoir permeability is too low. With insufficient nutrients present for methanogens to utilize, MECBM wells will not be economically viable. Hence, MECBM strategies for success are mainly focused on: 1) Development of effective nutrient recipes; 2) Increasing microbial access to coal and amendments; and 3) Promotion of nutrient injection. The overarching goal of this study is focused on physically increasing fracture area for microbial colonization and the subsequent injection of nutrients.

Hydraulic fracturing is an effective method to access reservoirs, especially tight reservoirs, and to then improve oil/gas production. Based on the utility of hydraulic fracturing in conventional reservoirs, hydraulic fracturing is expected to be one potentially effective method to stimulate MECBM reservoirs. The newly generated fractures will not only provide sufficient surface area for microbial colonization, but also enhance the permeability of the coal seam for nutrient delivery. Many classic fracture models have been proposed, including PKN, KGD and penny-shaped crack models, to investigate fracture propagation during fluid injection (Nordgren, 1972; Geertsma and Klerk, 1969; Green and Sneddon, 1950). Various methods based on techniques, such as non-invasive imaging and transport of tracers, have been proposed to characterize the roughness of fracture surfaces using parameters such as joint roughness coefficient (JRC), the root-mean-square of the fracture profile wall slope (Z_2) and fractal dimension (D_f) (Crandall et al., 2010; Huang et al., 2018). However, different from shales, coal is typically a more permeable medium with a potentially well-developed natural fracture network, which results in a strong anisotropy of the mechanical behavior of coal masses (Liu et al., 2018; Zhao et al., 2018). With the existence of natural fractures, propagation of hydraulic fractures is commonly influenced by the in-situ stress state, material properties, viscosity and injection rate of the fracturing fluid, fracture geometry, and reservoir permeability (Huang et al., 2017; Liu et al., 2014a; Rutqvist and Stephansson, 2003; Sammis and Ashby, 1986; Wang et al., 2018a,b). Recently, methods coupling porosity and permeability evolution with discrete fracture network (DFN) models to represent natural heterogeneity and anisotropy have been popular, using either equivalent continuum (Gan and Elsworth, 2016; Taron and Elsworth, 2010; Oda, 1986; Rutqvist et al., 2013) or discontinuum approaches (Ghassemi and Zhang, 2006; Min and Jing, 2003; McClure and Horne, 2013; Fu et al., 2013). Currently the investigation of hydraulic fractures in opening, propagating and in interacting with geologic

discontinuities, such as natural fractures, joints, faults and bedding planes, in a naturally fractured reservoir remains a challenge. Provided that coal has a lower strength than shale, proppant embedment in coal may play an important role in diminishing fracture conductivity. Proppant embedment, residual aperture and residual conductivity are all influenced by closure pressure, proppant size and concentration, fracture roughness, reservoir temperature, rock mineralogy and sorption behavior (Alramahi and Sundberg, 2012; Kumar et al., 2015; Lacy et al., 1998; Lee et al., 2010; Stephen and David, 2004; Zhang et al., 2013). Based on these observations, empirical expressions (Lacy et al., 1998; Volk et al., 1981; Wen et al., 2007) and analytical models (Guo et al., 2017; Jamari and Schipper, 2006; Kumar et al., 2015; Li et al., 2015) have been developed to characterize the response of propped fractures.

Descriptions of solute transport, including advection, diffusion, dispersion, sorption and chemical reaction, have been widely applied to understand the transport of solutes in reservoirs (Li et al., 2015; Liu et al., 2008; McGuire et al., 2013; Noiriel et al., 2010). In fractured rocks, the coupling of mechanical-hydrologic processes, including stress-induced changes in fracture apertures and poroelastic effects, exert a significant influence on transport properties. The compressive stress, for instance, can close fracture apertures and attenuate the dispersivity of solute components (Zhao et al., 2010). Dilated fractures will provide permeable flow pathways that result in high fluid velocities and accelerate mass transport. Effective stimulation in MECBM requires a broad sweep of the nutrient solution into the coal fracture-matrix system. This study explores such effects on solute transport in reservoirs with complex fracture geometries.

2. Mathematical formulation

Reservoir and hydraulic fracture-propagation modeling are completed through the implementation of a discrete fracture network (DFN) model to accommodate solute transport inside fractures and matrix as a process-coupled multi-continuum. We implement these models in TFReact (Taron and Elsworth, 2010; Taron et al., 2009a), a TOUGH-FLAC coupling simulator, to investigate nutrient transport with fracture-matrix interactions.

2.1. Fractured reservoir modeling

Coal is reasonably treated as an homogenous, isotropic and elastic continuum in many computational models (Liu et al., 2011; Rutqvist and Stephansson, 2003; Wang et al., 2013; Wu et al., 2011). The basic mechanical and hydraulic characteristics of fractures in coal may be interlinked through the theory of poroelasticity, viewed either as a single porosity or dual porosity medium (Biot, 1941; Elsworth and Bai, 1992; Zhi and Elsworth, 2016). However, the presence of pre-existing fractures requires coal to be represented as an elastic continuum intersected by a large natural fracture network, in which fractures are assumed as twin parallel fracture walls, connected by springs in both shear and normal deformation. Fig. 1 shows how a DFN in two orthogonal orientations may be represented using the finite difference method.

Discrete fracture networks (DFN) of natural fractures may be used to represent the major flow channels in realistic reservoirs. The complex fracture pattern yields the heterogeneity in the fracture permeability via the topology of the flow network. It is found that the distribution of DFN follows a power-law distribution, expressed in (Fang et al., 2015)

$$p(l) = \frac{\alpha - 1}{l_{min}} \left(\frac{l}{l_{min}} \right)^{-\alpha} \tag{1}$$

where $p(l)$ is the probability of fracture having a length l. l_{min} is the minimum fracture length. $(\alpha - 1)/l_{min}$ is the normalizing constant.

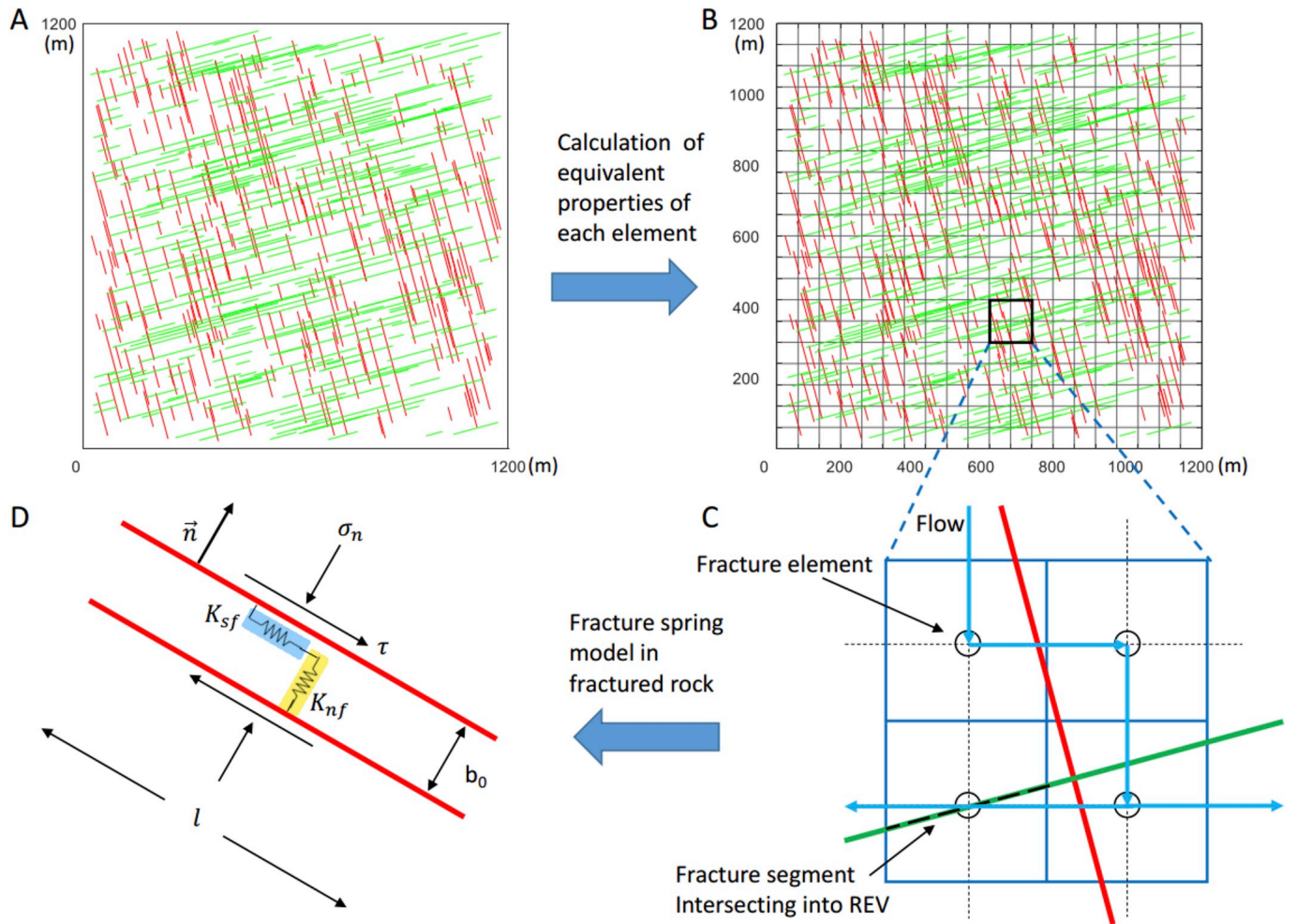The discrete fractures model is coupled with a continuum model to

Fig. 1. Scheme of the equivalent continuum method used in this study. (A) The original coalbed methane reservoir with DFN of two main orthogonal angles. (B) Mesh discretization used in finite differential method. (C) Schematic of how element properties influence fluid flow in the model. Red and green solid lines represent the discrete fractures. Light Blue solid lines represent the routines of fluid transport. (D) The fracture spring model.

represent the fractured mass. Based on the crack tensor theory proposed by Oda (1986), the equivalent bulk modulus K and shear modulus G in each multi-continuum element can be obtained as (Gan and Elsworth, 2016; Rutqvist et al., 2013)

$$K_{eq} = \frac{1}{\frac{1}{K_{intact}} + \sum_1^{fracnum} \frac{V_{ratio}}{b} \left[\left(\frac{1}{K_{nf}} - \frac{1}{K_{sf}} \right)(1 - n_2^4) + \frac{1}{K_{sf}} n_1^2 \right]}$$

$$G_{eq} = \frac{1}{\frac{1}{G_{intact}} + \sum_1^{fracnum} \frac{2V_{ratio}}{b} \left[\left(\frac{1}{K_{nf}} - \frac{1}{K_{sf}} \right)(n_1^4 - n_1^2 n_2^2) + \frac{1}{K_{sf}} n_1^2 \right]}$$

Where K_{nf} and K_{sf} are fracture normal stiffness and fracture shear stiffness, respectively. Vector $\mathbf{n}$ is the unit vector normal to each fracture.

In addition to the DFN models, the effect of poroelasticity is also integrated into the multi-continuum element. The relatively small-scale fracture system is considered homogeneously and isotopically distributed rather than being discretized as a DFN. Hence, the "matrix" in this modeling refers to a combination of both coal matrix and small partial fractures. The stress-strain relationship together with the consideration of fluid pore pressure p is

$$\varepsilon_{ij} = \frac{1}{2G}\sigma_{ij} - \left(\frac{1}{6G} - \frac{1}{9K} \right)\sigma_{kk}\delta_{ij} - \frac{\alpha}{3K}p\delta_{ij} + \frac{\varepsilon_s}{3}\delta_{ij} \tag{3}$$

where G is shear modulus, K is bulk modulus, ε_s represents sorption-

induced shrinkage or swelling. Considering the Biot coefficient $\alpha = K/K_s$, Eq. (3) can be expressed as

$$d\varepsilon_v = -\frac{dV}{V} = \frac{1}{K}d\bar{\sigma} - \left(\frac{1}{K} - \frac{1}{K_s} \right)dp + \varepsilon_s = \frac{1}{K}(d\bar{\sigma} - \alpha dp) + \varepsilon_s \tag{4}$$

where ε_v is the volumetric strain, $\bar{\sigma}$ is the hydrostatic stress.

2.2. Fracture opening model

Normal closure results from far-field stress and fluid pressure within the fracture. The reverse process to normal closure is hydraulic dilation during injection phase, as shown in Fig. 2. Based on the simplified Barton-Bandis hyperbolic-closure model, the aperture change can be formulated as (Baghbanan and Jing 2007; Gan and Elsworth, 2016)

$$b = b_0 - \frac{9b_0\sigma_n'}{\sigma_{nc} + 10\sigma_n'} + \frac{\tau - \tau_{fric}}{K_{fs}}\tan\phi_d + \frac{p_f - \sigma_n}{10 \times \frac{7\pi}{24}\frac{G}{r}} \tag{5}$$

where σ_{nc}, the critical normal stress, is assumed as $\sigma_{nc}(MPa) = 0.487b_0(\mu m) + 2.51$. σ_n' is the effective normal stress and b_0 is the initial aperture. τ_{fric} is the shear friction defined by $\tau_{fric} = S + \mu(\sigma_n - p_f)$, S is shear strength of the fracture, μ is friction coefficient, K_{fs} is fracture shear stiffness and ϕ_d is dilation angle. G is the shear modulus of intact rock and r is the fracture half length.

In this modeling, the volumetric strain is employed to independently calculate the porosity of the matrix and fracture. The
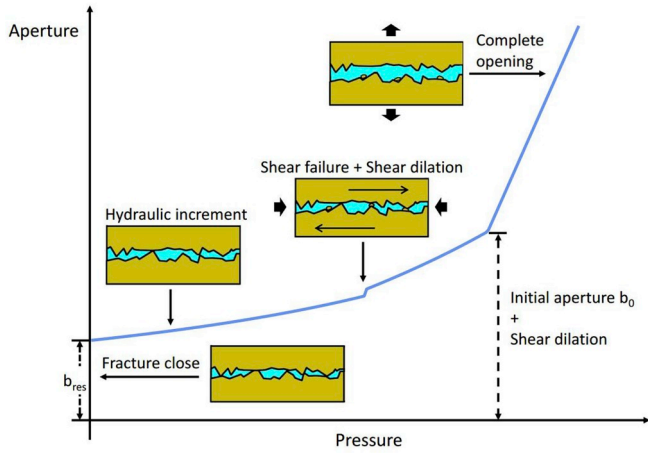
Fig. 2. Schematic of the pressure-aperture model.

equation that updates the porosity of matrix is written as (Chin et al., 2000):

$$\phi_{t+1}^m = 1 - (1 - \phi_t^m)e^{-\Delta\varepsilon_v^m} \tag{6}$$

where ε_v^m is the volumetric strain of the matrix with matrix porosity ϕ_t^m at time step t. A similar equation applies in evaluating the change in fracture porosity.

For a homogenous and isotropic continuum, the cubic law is typically adopted as the porosity-permeability relation for both matrix and fracture permeability evolution. The permeability of discrete fractures can be evaluated from the explicit fracture volume inside each mesh block. For an element containing a DFN, fracture permeability can be expressed as a sum of the permeability of the minor fractures in the matrix domain and the directional discrete fracture permeability. Hence, the integrated fracture permeability can be calculated as (Oda, 1986; Seidle and Huitt, 1995)

$$k_{ij} = \left(1 + \frac{\Delta\phi_f}{\phi_{f0}}\right)^3 k_{f0} + \sum^{frac_{num}} \frac{1}{12}\left(\frac{V_{ratio}}{b_0}b^3 n_k^2 \delta_{ij} - \frac{V_{ratio}}{b_0}b^3 n_i n_j\right) \tag{7}$$

where k_{ij} is the calculated tensor of fracture permeability, V_{ratio} is the fraction of the discrete fracture volume in the element volume, n is the unit normal to each fracture, $frac_{num}$ is the total number of the truncated fractures in each element and δ_{ij} is the Kronecker delta.

Proppant is usually pumped into opened hydraulic fractures after a certain period of water injection to maintain a reasonable fracture conductivity for the subsequent production stage. The choice of aperture opening model in the hydraulic fracture is different from that in the natural fracture. Fig. 3 shows the residual aperture due to proppant subjected to an applied normal stress in a hydraulic fracture. Residual

aperture of the proppant-supported fracture is often regarded as a function of the embedment and deformation of proppants.

Considering proppant embedment into coal and proppant deformation $\Delta D_2 = \frac{\sigma'}{E_2}D_2$, the propped aperture of hydraulic fracture can be calculated as (see Appendix A for a complete derivation and validation)

$$b = b_0 - 2R\left(1 - \sqrt{1 - \frac{\sigma'}{\pi C}}\right) - \left(\frac{\sigma'}{E^*}(1 - R_m) + \frac{\sigma'}{E_2}\right)D_2 \tag{8}$$

where b_0 is the initial aperture, here equal to D_2, the initial height of the proppant pack, R_m is the elastic modulus reduction ratio, σ' is effective stress applied on the flat surface and C is cohesive strength of the surface material. For a multi-layer propped fracture, aperture change can be approximated by superposition of the deformation of each proppant layer plus the embedment from the mono-layer, since only the top-layer and bottom-layer proppants directly contact coalbed and can be embedded (Li et al., 2015).

2.3. DFN application

A DFN of natural fractures (NF) and hydraulic fractures (HF) may be used to represent the major flow channels in a realistic reservoir. When a hydraulic fracture intersects a discrete natural fracture during its propagation, the fracturing fluid will invade into the connected natural fracture or fracture networks. It is assumed that the fluid pressure will quickly build up inside the natural fracture due to its high permeability. The nearest fracture branch tips will continue propagating as long as the propagation criterion is met. Fluid leak-off from all the connected natural fractures are calculated. Once the injection is completed, an evenly-paved proppant distribution is assumed inside the hydraulic fracture and the connected natural fractures of limited length.

The HF−NF geometry in the propagation processes is generated using the PKN model with a simplified fracture propagation criterion (Erdogan and Sih, 1963; Zhang and Jeffrey, 2014). Each fracture wing is generated accommodating mass conservation via a finite difference method. The fracture propagation criterion is based on the theory of linear elastic fracture mechanics (LEFM). A mixed stress intensity factor along the propagation direction is required to exceed the toughness at the onset of quasi-static crack growth. When the compression-shear wing cracks initiate under high fluid pressure, the mixed stress intensity factor at the wing crack tip can be simplified into a superposition of the two stress intensity factors, as shown in Eq. (14):

$$K_{IC} \geq K_I + K_{II} \tag{9}$$

where K_{IC} is fracture toughness of the material. The stress intensity factor at the crack tip can be obtained as (Liu et al., 2014a; Liu et al., 2014b):
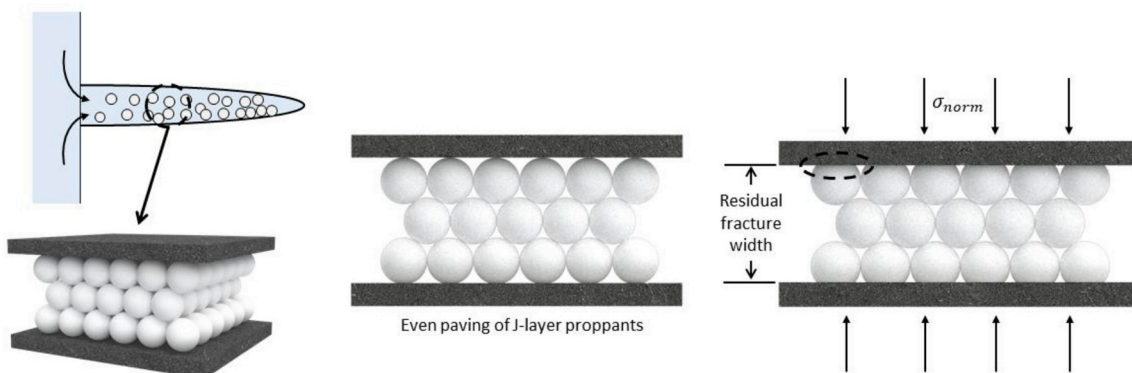

Fig. 3. Schematic of proppant embedment and residual fracture width within an hydraulic fracture.

$$K_I = \frac{2}{\sqrt{3}}\sigma_n'\sqrt{\pi a} = \frac{2}{\sqrt{3}}(\sigma_n - p_f)\sqrt{\pi a}$$

$$K_{II} = \frac{2}{\sqrt{3}}(\tau - \mu_f\sigma_n')\sqrt{\pi a}$$

Where μ_f is friction coefficient. When fluid pressure exceeds the normal stress applied on fracture wall, the friction force is null. Since the principle of fracture propagation is for the evolving feature to follow the path of least resistance (Daneshy, 2003; Liu et al., 2014a; Liu et al., 2014b), the critical fluid pressures P_{fc}, in Eq. B1 and B3, for the initiation of wing fractures and for fracture crossing are then compared to determine whether wing fracture extension or fracture crossing will occur.

After satisfying the propagation criterion, a fracture model following a PKN-formalism and based on FDM is used to estimate the propagation of the hydraulic fracture during ongoing injection. Local fluid flow in the dilating HF portion is based on the lubrication equation. The global mass conservation is based on the principle that the volume of the injected fluid is equal to the volume of the fracture and the cumulative leak-off volume (Detournay et al., 1990). The generated fracture length L can be obtained by solving the global equation

$$\int_0^{L(t)} \omega(x,t)ds + \int_{t_0(x)}^t \int_0^{L(t_0)} u(x,\tau)dx\,dt = \int_0^t q_0(t)dt \tag{11}$$

For the wing fractures that initiate from the tips of a pre-existing fracture, the equation above can be written as

$$\int_0^{L_{n0}+L_n(t)} \omega(x,t)dx + \int_{t_{n0}(x)}^t \int_0^{L_{n0}+L_n(t)} u(x,t)dx\,dt = \int_{t_{n0}(x)}^t q_{n0}(t)dt \tag{12}$$

where n denotes fracture propagation index and t_{n0} is the start time of the *n-th* fracture branch and t is the arrival time of the *n-th* fracture tip at location x. L_{n0} is the total fracture length connected with the new branch. The derivation and validation of the proposed PKN-based model can be found in Appendix B.

2.4. Solute transport

We represent solute transport through conservation of dissolved mass in a porous medium using the flow equation to define Darcy velocity

$$\frac{\partial M_k}{\partial t} = -\nabla F_k + Q_k \tag{13}$$

where $\Delta M = \Delta(\phi\rho)$ is fluid mass accumulation, F is mass flux from Darcy's law, and Q is mass source/sink. The subscript k is phase index for flow.

Solute transport includes advection, diffusion and dispersion. In a porous medium, the effect of diffusion is generally smaller in comparison to the dispersion process. Hence, the hydrodynamic dispersion coefficient D is typically adopted as a summation of the mechanical dispersion coefficient D_m and the effective diffusion coefficient D_e. In 2D systems, the general Advection-Dispersion Equation (ADE) is:

$$\frac{\partial M_k}{\partial t} = -\nabla\cdot(\boldsymbol{u}C_{jk} - D\nabla C_{jk}) + Q_k \tag{14}$$

where C_{jk} is the tracer concentration for the *j-th* component and $\boldsymbol{u}$ is Darcy velocity.

3. Simulation design

A prototypical MECBM reservoir under in-situ stresses and 1200 m × 1200 m × 10 m is used in this study. Three cases are simulated to compare fluid flow and solute transport for different scenarios. Both natural and hydraulically-driven fractures are represented by a DFN coupled into the multi-continuum model. The following defines how these models are assembled.

3.1. Biogeochemical controls

Most methanogens commonly inhabiting coalbed reservoirs are members of a single phylum, the Euryarchaeota, belonging to the domain of Archaea (Lloyd, 2015). In addition to methanogens, the collective actions of fermentative and acetogenic bacteria are required for microbial bioconversion from coal to methane. First, the complex organic matter in coal is decomposed to simpler molecules, i.e., acetate, long chain fatty acids, and HS^-, by fermentative anaerobes. Fatty acids, alcohols, and some aromatic and amino acids are then transformed to H_2, CO_2, and acetate by H_2-producing acetogens. Eventually, those simple molecules are converted to CH_4 by methanogens (Faiz and Hendry, 2006). All the microbial communities involved in methanogenesis are ubiquitous and in elevated concentrations in the formation water and coal in biogenic coalbed methane reservoirs (Stolper et al., 2014; Zhang et al., 2015). In this study, the presence of these necessary microbial communities promoting methanogenesis is presumed in the stimulated coalbed methane reservoir.

Coalbed methanogens, if properly nurtured, can increase methane production from existing wells. Typical nutrient recipes comprise four major ingredients: 1) mineral solutions, such as: Mg^{2+}, Ca^{2+}, Na^+ and K^+; 2) vitamin solutions, such as: vitamin B12, thiotic acid and nicotinic acid; 3) trace metal elements, such as: B, Zn, Co, Mo and Fe; 4) organic matter, such as: yeast extract and peptone as nitrogen sources (Green et al., 2008; Zhang et al., 2016b). Given the high hydraulic gradient that is present between injection and the far field within reservoir, flows are advection dominated with mechanical dispersion and diffusion mechanism of the prevailing mixing. Thus, differences between diffusion coefficients of the various solutes in the nutrient recipes are negligible and hydrodynamic dispersion dominates mixing at the solute front. Therefore, the injected nutrient is considered as a tracer and its concentration is normalized to 1.0 (the optimal condition for nutrient).

3.2. DFN generation of natural fractures

Discrete fracture networks with appropriate mechanisms coupling mechanical response play a significant role in understanding how a connective fracture system channels fluid flow (Long and Witherspoon, 1985). Two sets of discrete fractures are constructed at azimuths (from the North) of 075° and 165° in a 1200 m × 1200 m × 10 m coalbed methane reservoir. Since the length of each individual fracture is set in the range of 40–300 m and $\alpha = 1.5$, the equation of this power-law distribution becomes

$$p(x) = 0.025\left(\frac{x}{20}\right)^{-1.5} \tag{15}$$

where p(x) is the probability for a single fracture of length x. In total 200 fractures (100 fractures for each orientation of two sets) are randomly distributed in the simulated domain. A natural fracture system comprises smaller fractures representing local fractures/joints and larger fractures representing large-scale geological faults in the coal seam. In this DFN modeling, minor natural fractures with lengths < 40 m are incorporated into the matrix domain in the multi-continuum element using an equivalent continuum approach. Fig. 4 shows a histogram of the fracture probability distribution for one fracture set.

Initial aperture b_i for each fracture is proportional to its length l, following a power law function (Gan and Elsworth, 2016; Ghanbarian et al., 2018; Olson, 2003). Distribution of the initial fracture aperture is plotted in Fig. 5. Heterogeneity of the natural fracture network has been incorporated into the properties of the multi-continuum elements. Initial fracture porosity and permeability are calculated based on the properties of both the fracture and matrix. Initial fracture porosity is the ratio between the overall fracture volume within the single element and
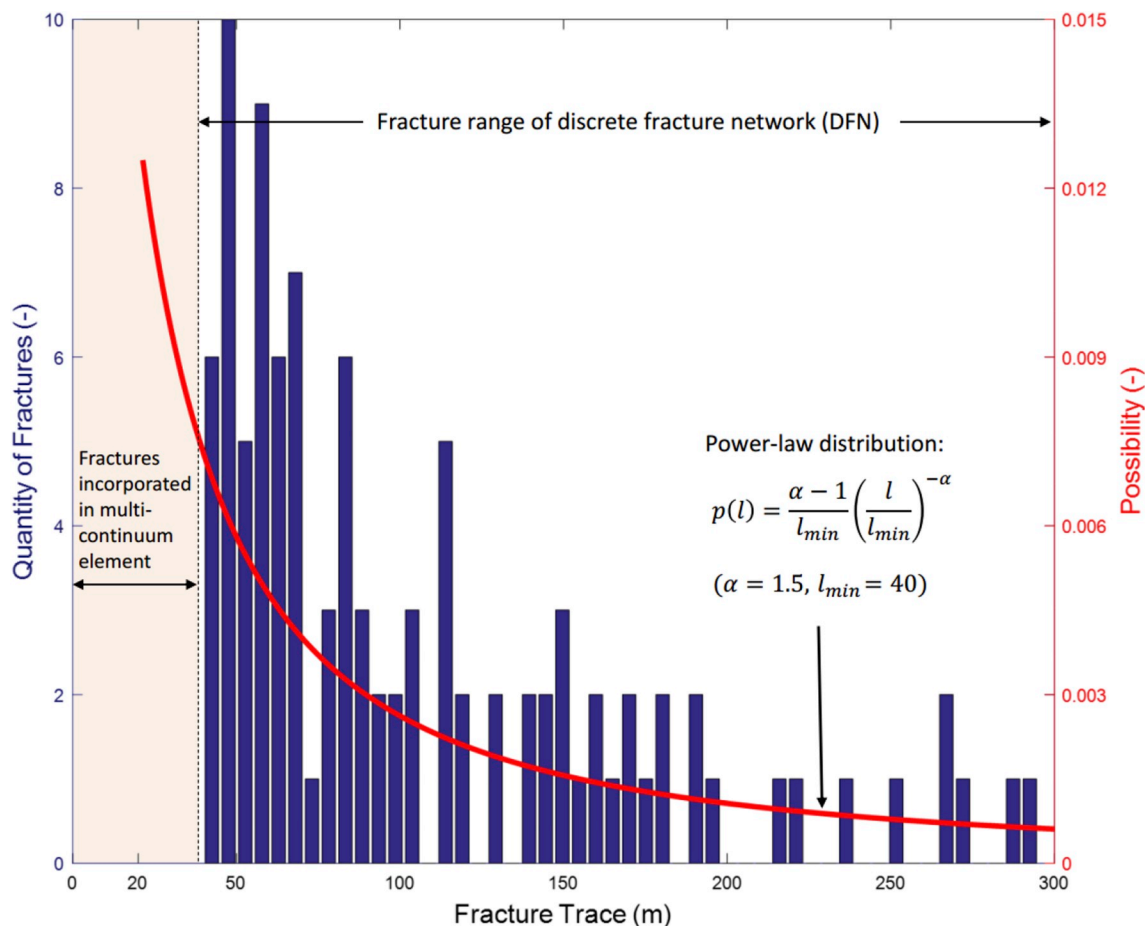
Fig. 4. Histogram of fracture lengths and their probability distribution for an example of 100 fractures.
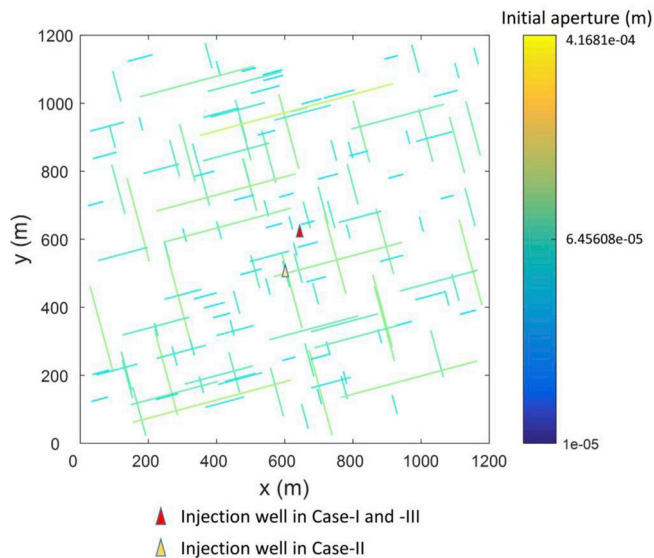

Fig. 5. Distribution the initial apertures of the two sets of discrete fractures.

the entire element volume. Initial fracture permeability is calculated using Eq. (9) with the fracture porosity determined in the prior time/iteration step.

3.3. Characteristics of example cases

Key modeling parameters properties in this study are listed in

Table 1
Modeling parameters for the numerical simulation.

Parameter	Value
Young's modulus of coal (E)	2.45 GPa
Poisson's ratio of coal (ν)	0.3
Density of coal (ρ_c)	1220 kg/m^3
Fluid dynamic viscosity (μ)	$0.653 \times 10^{-3} Pa \cdot s$
Temperature (T)	313.14 K
Injection pressure (P_f)	14 MPa
Maximum confining stress (σ_1)	20 MPa
Minimum confining stress (σ_3)	16 MPa
Initial reservoir pressure (P_{f0})	1.0 MPa
Fracture angle (θ)	75/-15°
Initial matrix permeability (k_{mo})	$1.0 \times 10^{-17} m^2$
Initial fracture permeability (k_{fo})	$0.5 \sim 2.5 \times 10^{-16} m^2$
Initial joint normal stiffness (k_n)	5 GPa/m
Initial joint shear stiffness (k_s)	50 GPa/m
Biot's coefficient (α)	0.9
Simulation time (t)	30 day

Table 1. The maximum and minimum principal stresses are set to 20 MPa (E-W direction) and 16 MPa (N−S direction), respectively. Before injection, an initial reservoir pressure of 1 MPa is assigned to represent depleted fluid pressure in the reservoir due to prior water and gas production. In the default scenario, injection pressure is set to 14 MPa, which is close to the closure stress applied on the hydraulic fractures.

The layout of the injection well is also shown in Fig. 7. In Case-I and −III, the injection wells are located in the same position, approximately 50 m out from the neighboring DFN. The injection well for Case-II is

Table 2
Modeling parameters for hydraulic fracturing.

Parameter	Value
Young's modulus of coal (E)	2.45 GPa
Poisson's ratio of coal (ν)	0.3
Fluid dynamic viscosity (μ)	0.05 $Pa{\cdot}s$
Injection flow rate (Q_0)	0.03 m^3/s
Coal seam thickness (h)	10 m
Leak-off coefficient (C_L)	$1 \times 10^{-6} m{\cdot}s^{0.5}$
Cohesion (C)	3.0 MPa
Biot's coefficient (α)	0.9
Simulation time (t)	100/500/1500/2500 s

sufficiently close to a long fracture oriented at an azimuth of 075° within the fracture network. This results in the injection well being connected to the pre-existing permeable fracture networks. To summarize, the injection wells are located at (650,610) in Case-I and −III, and at (610,510) in Case-II. The first two cases are used to examine the effects of mass transport using matrix and the natural fracture network stimulated at below the minimum principal stress, respectively. Case-III is for stimulation of the naturally fractured reservoir by hydraulic fracturing.

3.4. Hydraulic fracture propagation

As discussed previously (Section 2.3), the mechanics of fracture initiation is based on LEFM theory using a toughness criterion. Wing fractures grow when the mixed stress intensity factor along the propagation direction is equal to the toughness at the onset of quasi-static crack initiation (Erdogan and Sih, 1963). A commonly used PKN model is adopted to shape the generated hydraulic fractures. The modeling properties used in this propagation method are shown in Table 2. The propagated length of the hydraulic fracture is calculated by solving the global equations Eq. (26) and Eq. (27) in MATLAB. In terms of interaction with natural fractures, it is assumed that the hydraulic fractures have identical leak-off behavior to the pre-existing natural fractures. The propagation of hydraulic fractures in case-III is illustrated in Fig. 6. The blue solid lines represent the bi-wing hydraulic fractures and propped natured fractures. The arrays of short blue bars represent pressure profiles at specific times. The pressure profile above each hydraulic fracture is defined at the moment when it interacts with the DFN.

4. Results and discussion

Here we present a prototypical MECBM represented by a pseudo 3D model domain of 1200 m × 1200 m × 10 m at isothermal conditions of 40 °C. As introduced above, a maximum principal stress (E-W direction) of 20 MPa and a minimum principal stress (N−S direction) of 16 MPa are applied on the lateral boundaries. A vertical stress of 24 MPa is applied on the top as the overburden. Boundary conditions are applied at time $t = 0^-$ to equilibrate with initial pore pressure of 1 MPa. The injection pressure is set constant in time at 14 MPa in all three cases.

4.1. Concentration distribution

After injection for 30 days, the distribution of relative concentrations (RC) in the three cases are shown in Fig. 7. Note that there is no discrete fracture near the inlet in Case-I, although permeability of the small fractures (< 40 m) in the non-discretized matrix have been considered as $k = k_m + k_f$. Hence, solute transport is only dependent on the matrix diffusion in Case-I. Clearly, the solute in Case-I is delivered the shortest distance and spreads over the smallest area among the three cases. Nutrient distributions of the other two cases demonstrate a map of penetration that is strongly shaped by DFN geometry. Cases-II and

−III demonstrate that the discrete fractures play a pivotal role in solute transport. The pre-existing fracture network dramatically enhances the solute transport in Case-II when compared to Case-I. In Case-III, the penetrated area of the reservoir is dominated by the newly-generated hydraulic fractures in the E-W orientation. The resultant flow pattern is influenced by the interconnected HF−NF network, which has a larger reach than in the case of the pristine NF network in Case-II. Fig. 8 illustrates how the relative concentration evolves with the duration of injection in Cases-II and −III. The saturated area of RC > 0.1 in Case-III is larger than that in Case-II, especially after the first day of injection - due to the higher permeability of the propped hydraulic fractures. Comparing 30-day injection with the 1-day and 15-day injections, the spreading rates of the high-concentration areas in both cases reach their maximum in the early stage of injection and then the rate of growth gradually declines with continuing injection. This is because the reservoir pressure gradually equilibrates to the injection pressure and thus advective transport is replaced by diffusion.

To illustrate the solute flow path during injection, a cross section through the injection well in the E-W direction is chosen to construct cross-sections of relative concentrations, shown in Fig. 9. Fig. 9(A) shows an approximately symmetric distribution of mineral concentration due to the homogeneity of the matrix near the injection well in Case-I. However, asymmetric distributions of solute concentration can be seen in the other two cases because of the presence of the DFN. A steep concentration gradient evolves from the inlet to the plume front after the first day in Case-I, while the surrounding areas gradually become fully saturated after 30 days. However, only 70 m outward from the injector is permeated at RC > 0.8 when the injection ends. Fig. 9(B) shows solute transport via the coal matrix which is strongly influenced by the adjacent natural fracture networks. In case-II, solute first is transported through the connected natural fracture network. Then, the high-concentration solute in the fractures is carried to the nearby matrix by the hydraulic gradient between the fracture and matrix. After 30-days of injection, solute of RC > 0.8 is transported to about 100 m and 50 m from the injector in the East and West directions, respectively. The natural fracture connected to the injector shows a strong influence until the flow reaches the end of the fracture in the E-W direction. Fig. 9(C) illustrates the enhancement in nutrient delivery that evolves inside the hydraulic fractures. Different from the angled nature fractures, the hydraulic fractures in Case-III have the same orientation with the maximum principal stress. After 10-days of injection, the relative concentration curve is remarkably flat near the injection well instead of replicating the steep gradients of Cases-I and −II. This reveals that along the cutting direction, the 10th-day of injection after hydraulic fracturing results in a better nutrient delivery than after 30-days of injection in Case-I. After 30-days of injection, the nutrient concentration reaches full saturation from −140 m to 130 m in the cross-cutting direction. A moderate decline occurs in the range −170 m to −420 m due to mass transport from the propped natural fractures. A steep drop of RC occurs for propagation in the opposite direction because the HF propagation ceases at a NF oriented at an azimuth of 165°. The spiked-shape of the concentration profiles in Fig. 9(B) and (C) results from intersections between the section and the fracture networks. This shows that indeed the nutrient is readily and effectively transported along a tortuous fracture network.

The heterogeneity of the concentration distribution (Fig. 9 A, B and C) demonstrates the influence of the three different media on solute transport - coal matrix (Case-I), the natural fracture network (Case-II) and the NF network stimulated by hydraulic fracturing (Case-III). Since there are two different fracture sets comprising the natural fractures in the simulated coal reservoir, totally four types of media are investigated, as shown in Fig. 12. Locations that are 80 m outward from the inlet are selected to monitor the evolution of concentration. The red curve at the top shows a typical pattern of concentration evolution for a newly-generated hydraulic fracture. Concentration in the hydraulic fracture increases exponentially after injection begins and then
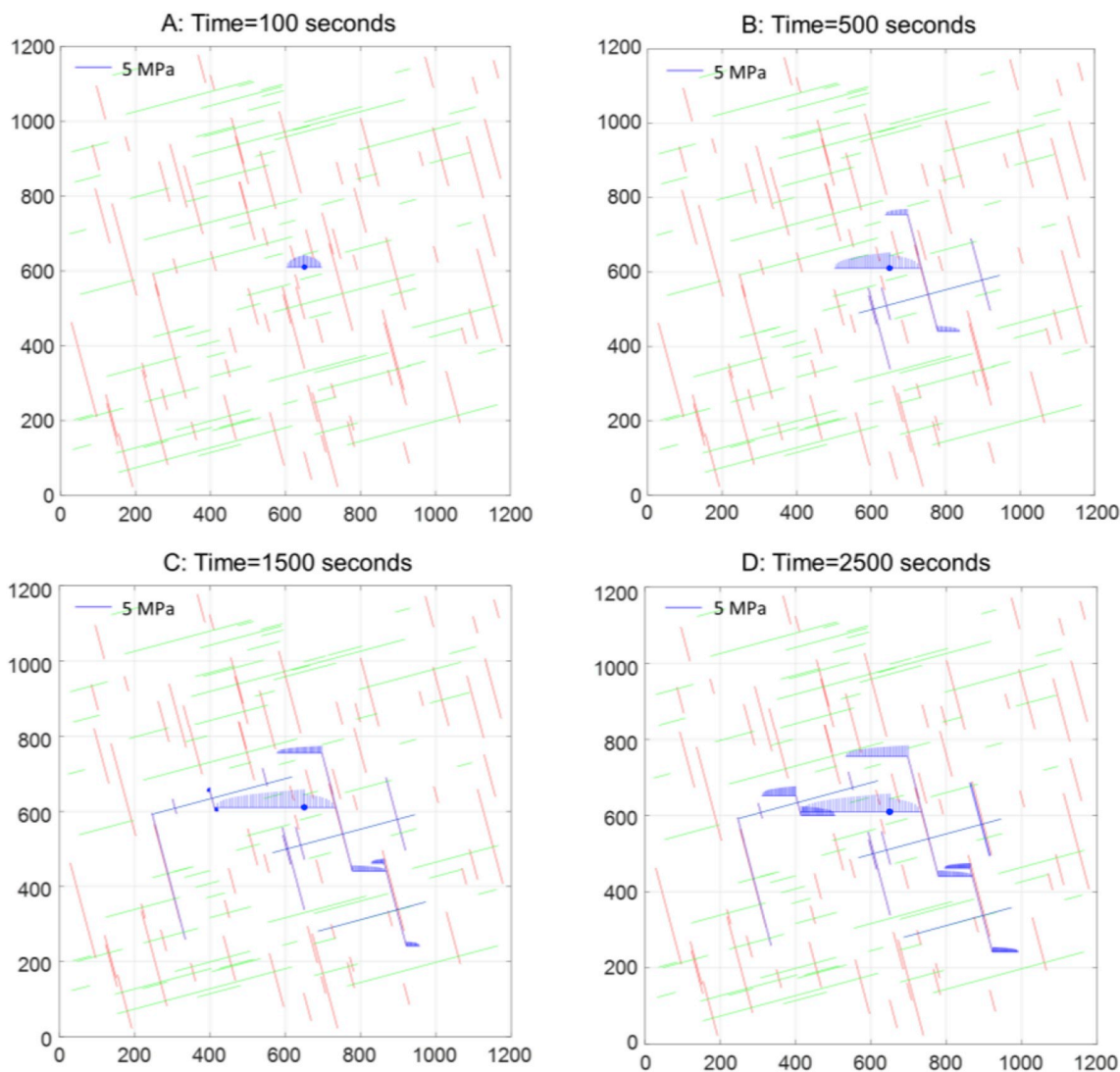
Fig. 6. Propagation of hydraulic fractures at different times in case-III. The blue solid lines represent the bi-wing hydraulic fractures and natured fractures into which proppant has washed. The arrays of short blue bars represent pressure profiles at certain injection times. The pressure profiles are defined at the moment they interact with the DFN.

gradually reaches an equilibrium concentration (RC = 1.0). In this case, relative concentration reaches 0.8 and 0.5 only after 5.4 and 10.9 days of injection, respectively. The slowdown in the rate of growth is primarily caused by the reduced advection in the hydraulic fractures. The two blue curves represent two different patterns of concentration accumulation in pre-existing natural fractures. The upper solid blue
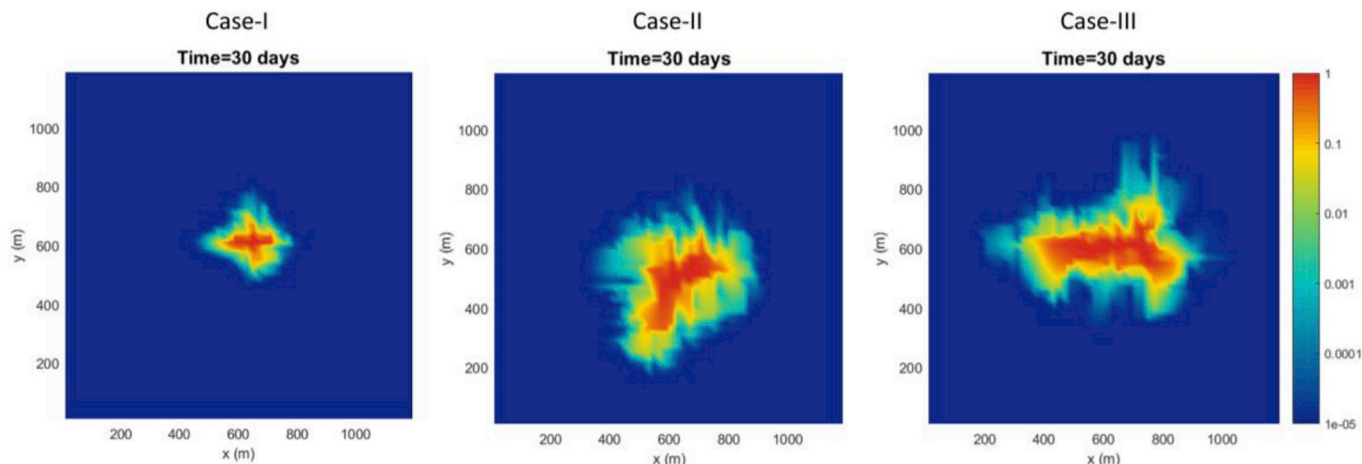
Fig. 7. Relative concentration distributions in the reservoir after 30-days of injection for the three different cases.
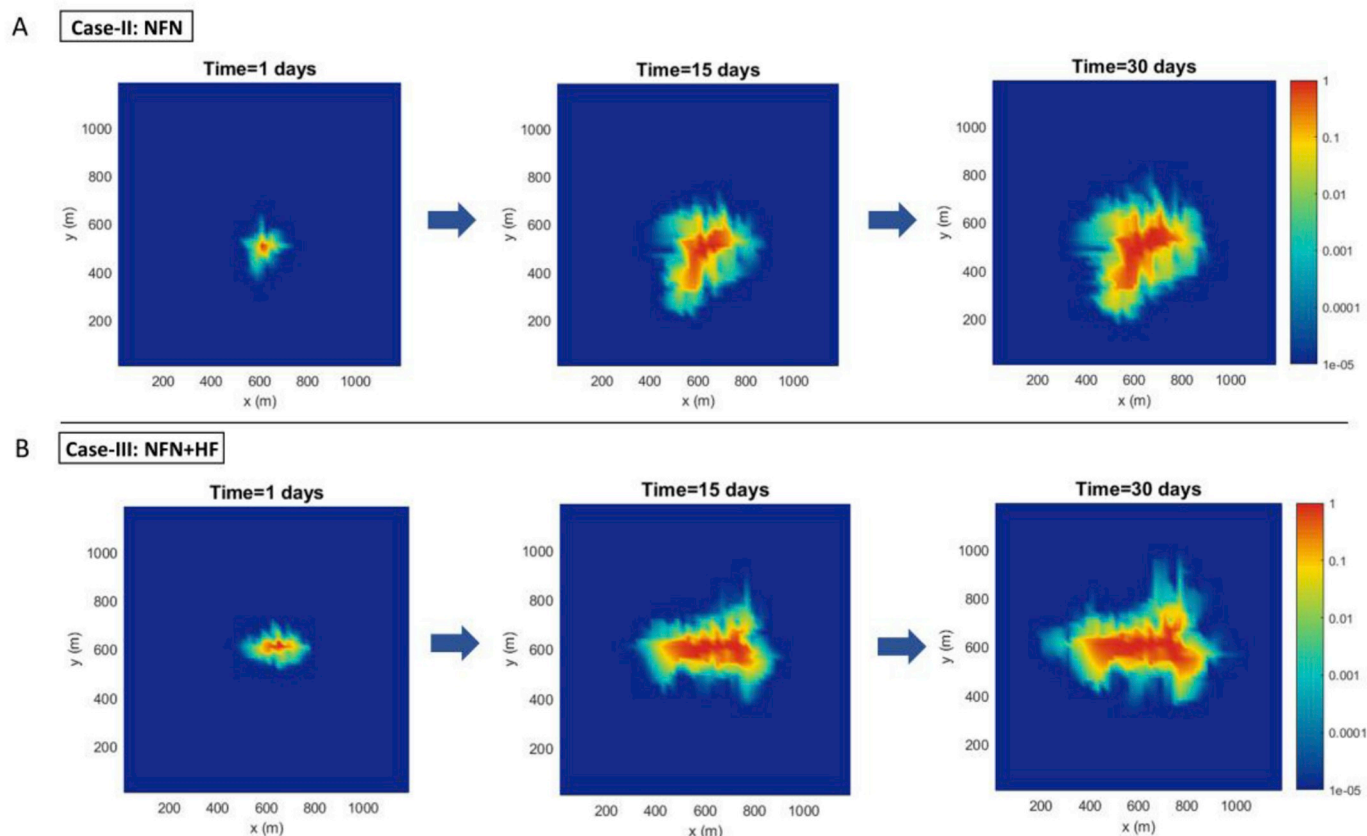
Fig. 8. Relative concentration distributions in the reservoir vs. injection time for Case-II and Case-III.

curve shows how solute concentration builds in the natural fracture oriented at an azimuth of 075°, oriented only at 15° to the maximum principal stress. The relatively smaller normal stress promotes the creation of a permeable pathway for solute transport and results in a rapid pressure build-up distant from injection. Therefore, the relative concentration increases rapidly and then gradually slows when RC > 0.75 (in this case) akin to that observed for the hydraulic fracture. The lower dashed blue line represents a distinctly different pattern of concentration growth in natural fractures that are subject to a larger normal stress. The larger restraining stress on the fracture walls induces a smaller initial fracture aperture and requires a higher opening pressure. Therefore, instead of increasing rapidly, the concentration initially grows only slowly. After fluid pressure rises and the fracture permeability increases, the rate of increase in concentration is gradually enhanced. The enhanced delivery capacity of the hydraulic fracture can be seen when compared to the natural fracture. The slow build-up of concentration in a nearly linear trend in matrix is also shown as the grey line in Fig. 10.

4.2. Nutrient abundance

In addition to the normalized tracer concentration, it is important to estimate the absolute mineral abundance that has been injected into the CBM reservoir. The evolution of cumulative injected nutrient volume is plotted using a logarithmic scale in Fig. 11 (A). The eventual injection volumes of nutrient in the three cases are 2.8×10^4 L, 1.23×10^5 L and 8.9×10^5 L, respectively. The influence of the fracture channel on nutrient delivery is distinct since the total injected volumes in Case-II and Case-III are ~4–32-fold larger than the base case. The accumulation rate of the injection becomes linear after a short period of injection. These phenomena can also be observed in Cases-II and −III. The evolution of injection rate at a constant injection pressure for each case is

shown in Fig. 11(B). The slope of the flow rate corresponds to the trend in cumulative injection volume. Due to its larger permeability, injection rate in the hydraulic fracture network is always higher than that in pre-existing fractures under the current configuration. Compared with Case-II, a larger maximum injection rate in Case-III is reached early and results in an approximately 8-fold increment of injection volume.

4.3. Saturated cleat area

Recent studies suggest that it is the coal cleat system where methanogens interact with the coal and injected nutrient (Ritter et al., 2015; Scott, 1999). The enhanced bio-gasification effect is dependent upon the area of the saturated cleat surface after nutrient injection. Although the macropore space (> 1000 nm) may also partially provide microbial access to bacteria, its effect is difficult to rigorously quantify due to the diversity of microbe species and sizes. Therefore, only the surface area of the cleat system and the DFN are considered in the evaluating the effective methanogenesis in this study. Fig. 12 shows the linear relation between cleat spacing and cleat surface area. For a cleat spacing of 10 cleat/inch (4 cleat/cm), the total cleat surface area will be 1.94×10^3 m²/ton, whereas a cleat spacing of 0.1 cleat/inch (0.4 cleat/cm) will have a cleat surface area of 19.36 m²/ton. This estimation is on the basis of an homogenous and isotropic cleat distribution. In this study, we assume an average cleat surface area of 600 m²/ton (2.5 cleat/inch). A concept of saturated cleat area (SCA) is introduced to investigate the saturation state of the treated reservoir. Cleat area saturated by solute is defined as a summation of the fracture surface area of the DFN and the average cleat surface area at a certain concentration. Four relative concentration tiers from > 0.0001 to > 0.1 at 10-fold intervals are used. For each multi-continuum element, SCA can be calculated by the following equation if the relative concentration in this element is larger than a certain threshold:
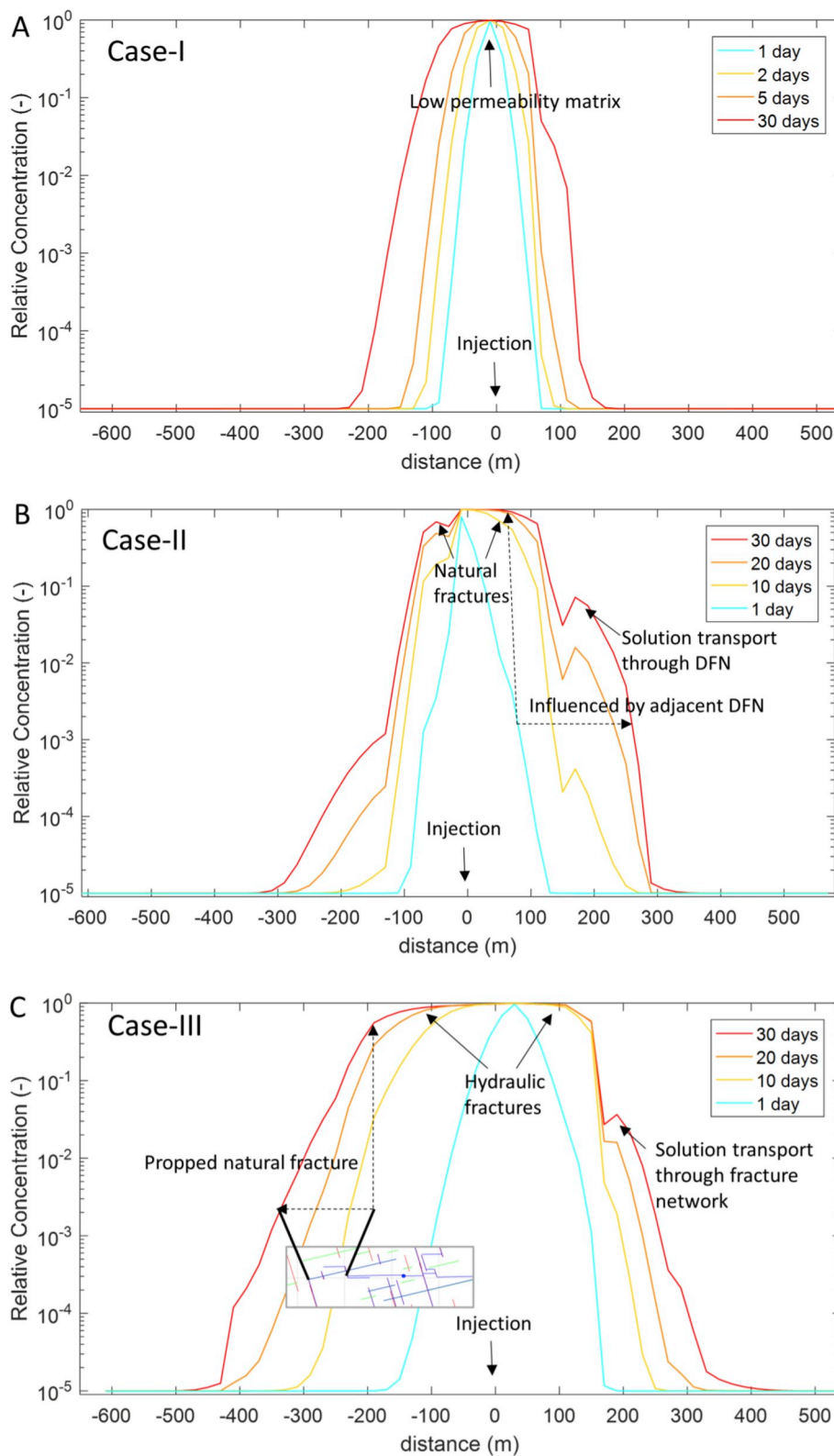
Fig. 9. A cross section through the injection well in the E-W direction in each case is chosen to construct cross-sections of relative concentrations. Changes in relative concentrations at 1 day, 10 days, 20 days and 30 days are shown for the three cases in (A), (B) and (C), respectively.

$$SCA = \sum_{n=1}^{frac_{num}} 2l_n h + A_0 V_e \rho \tag{16}$$

where $frac_{num}$ is the number of discrete fractures within the element, V_e is the element volume, l_n is the length of the n-th segmented fracture, A_0

is the average cleat surface area per ton of coal and ρ is coal density (here $1220 \, kg/m^3$).

Fig. 13 shows that SCA increases with injection time in the three modeling cases. In each RC range, the SCA rises at a faster rate at the beginning and then decreases to a flat linear trend. This reveals that the
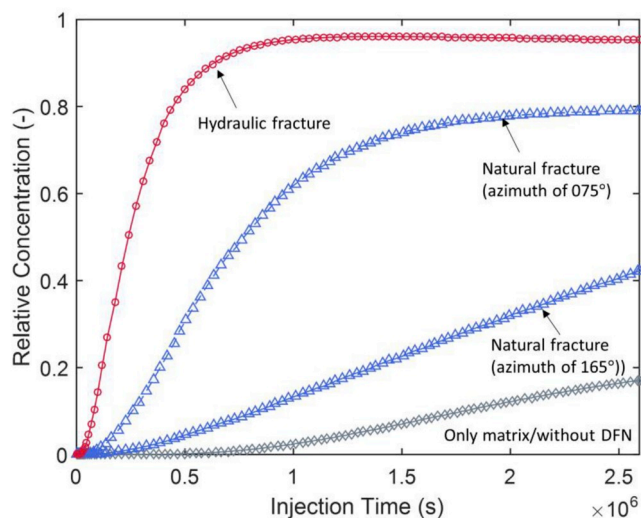
Fig. 10. Concentration evolution for different matrix/fracture types. All the monitored locations are 60 m outward from the injection well.

solute transport gradually changes from advection to diffusion. Each concentration tier sweeps approximately the same surface area in all cases. It is worth noting that the concentration tiers are at 10-fold intervals. This indicates that simply increasing nutrient concentration at inlet may have a low efficiency in increasing the swept surface area to an optimal concentration. After 30-days of injection, the hydro-fracturing case (case-III) provides a saturated surface area of 1.19×10^5 m^2 for RC > 0.1, while nearly half of this is only accessed (0.75×10^5 m^2) for Case-II. Not surprisingly, Case-I has the lowest saturated area of 1.63×10^4 m^2 for RC > 0.1. Fig. 13 (D) also shows that SCA increases slowly at the conclusion of the injection for RC > 0.1 in Case-II, whereas the retardation trend does not appear in any RC tier in Case-III. This is because the hydraulic fractures play an important role in delivering solute to the connected remote natural fracture system even at end stage of injection.

4.4. Proppant embedment

The effect of proppant embedment in hydraulic fractures is also investigated in this simulation. Large magnitudes of proppant embedment will result in compaction and fracture diagenesis of the newly-generated hydraulic fractures and impede their conductivity. Hence,
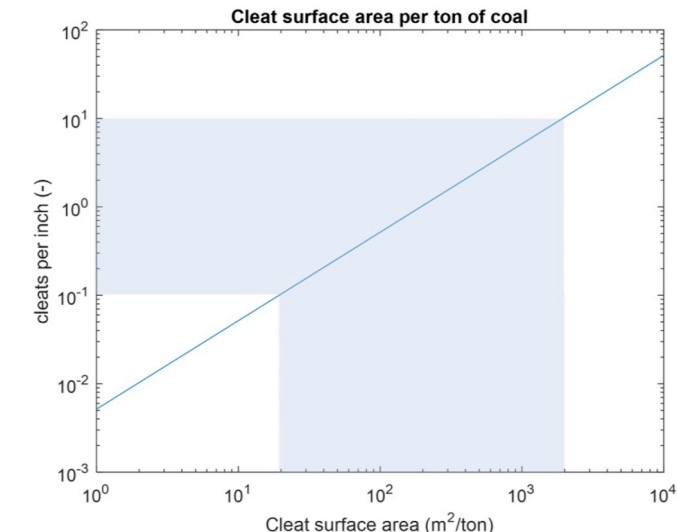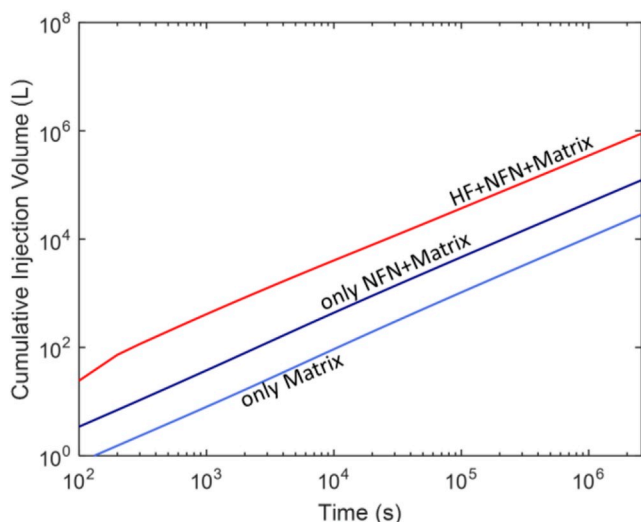

Fig. 12. Relation between cleat spacing and cleat surface area per ton of coal based on the assumption of an homogenous and isotropic cleat distribution. Macropore space (> 1000 nm) may also partially provide microbial access to bacteria, but its effect is difficult to be rigorously quantified. Hence, only the cleat surface area and surface of the DFN are considered for methanogenesis in this study.

solute transport within the fracture system will be significantly influenced by the indentation of proppant into coal matrix. From Eq. (13), the higher the cohesive strength C, the more difficult to penetrate the coal matrix in compression and thus the lower the proppant embedment. Fig. 14 shows how apertures near the inlet change with the duration of injection for different cohesive strengths. Cohesive strength of the coal is set to 2.0, 2.5, and 3.0 MPa for each scenario, respectively. Even distribution of a single-layer of proppant is assumed in all cases. The initial aperture before re-injection of the nutrient solution is 0.11 mm in the case for C = 2 MPa (larger proppant embedment due to weaker fracture wall), while the initial aperture before nutrient re-injection in the case of C = 3 MPa is 0.24 mm (stronger fracture wall). Clearly, with higher cohesion C, fracture aperture increases more quickly and finally reaches a larger maximum. It can be concluded that the aperture evolution curve in each case initially increases but then ceases when fluid pressures peak. The trend of permeability evolution is consistent with aperture evolution since the changes in aperture are fundamental in calculating fracture permeability in this modeling.
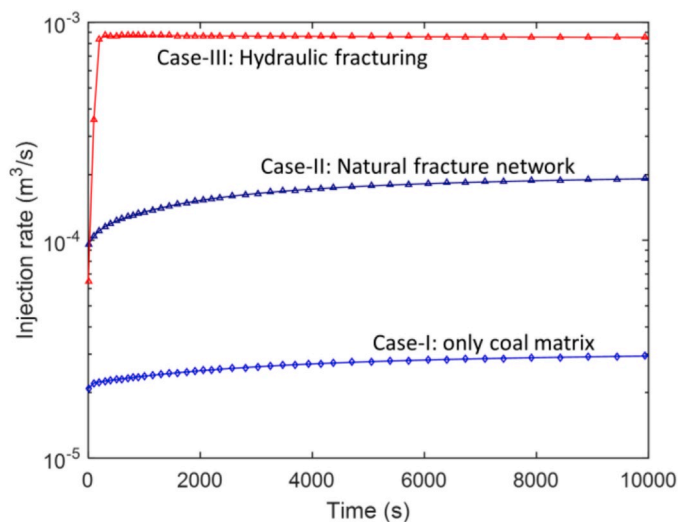

Fig. 11. (A) Cumulative injected volume of nutrient versus injection time; (B) Injection rates in first 10000 s injection (Injection pressure is set to 14 MPa).
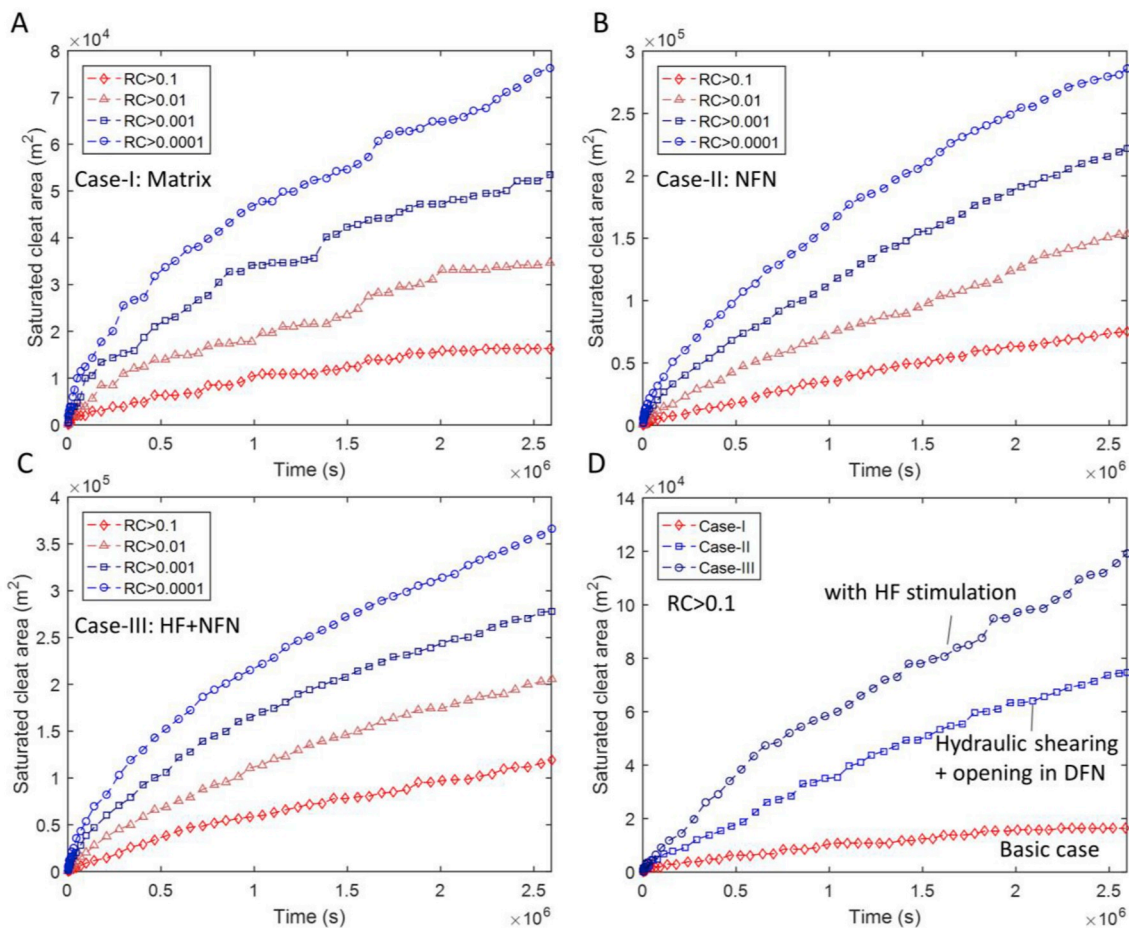
Fig. 13. Saturated cleat area (SCA) increases with injection time in the three modeling cases. Four concentration tiers are used in the range of RC from > 0.00001 to > 0.1 at 10-fold intervals.

Fig. 15 shows the permeability distribution and pressure distribution for different cohesions, C, both before and after 30 days of injection. Before injection, the maximum initial permeability of hydraulic fractures is $3.1 \times 10^{-16} m^2$ and $8.9 \times 10^{-16} m^2$ in cases of $C = 2$ and 3 MPa, respectively. After 30 days of injection, the maximum fracture permeability is raised to $8.0 \times 10^{-14} m^2$ in the case of $C = 3$ MPa, but
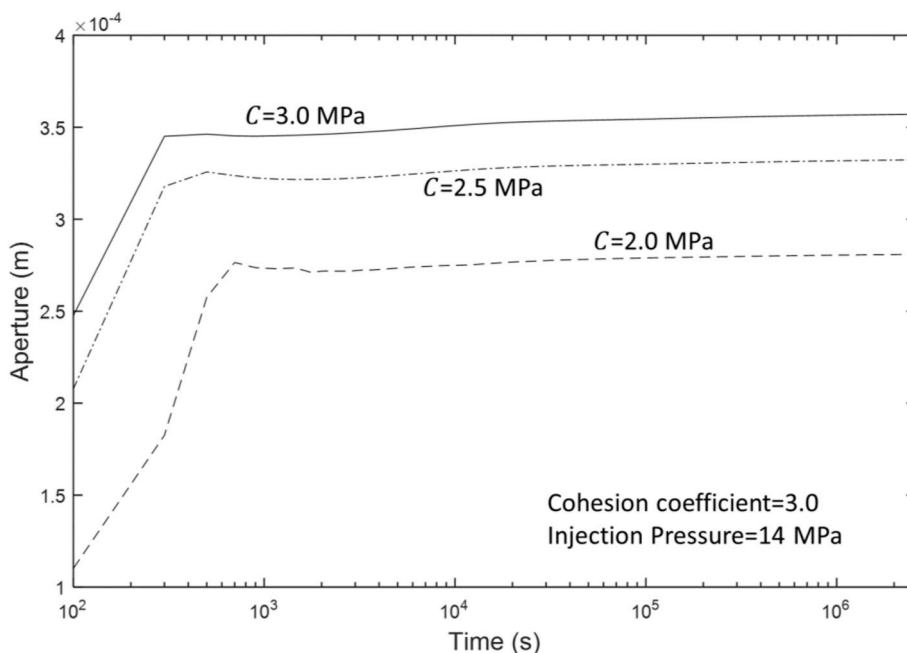

Fig. 14. Aperture evolution near the inlet for the cases with different cohesion C.
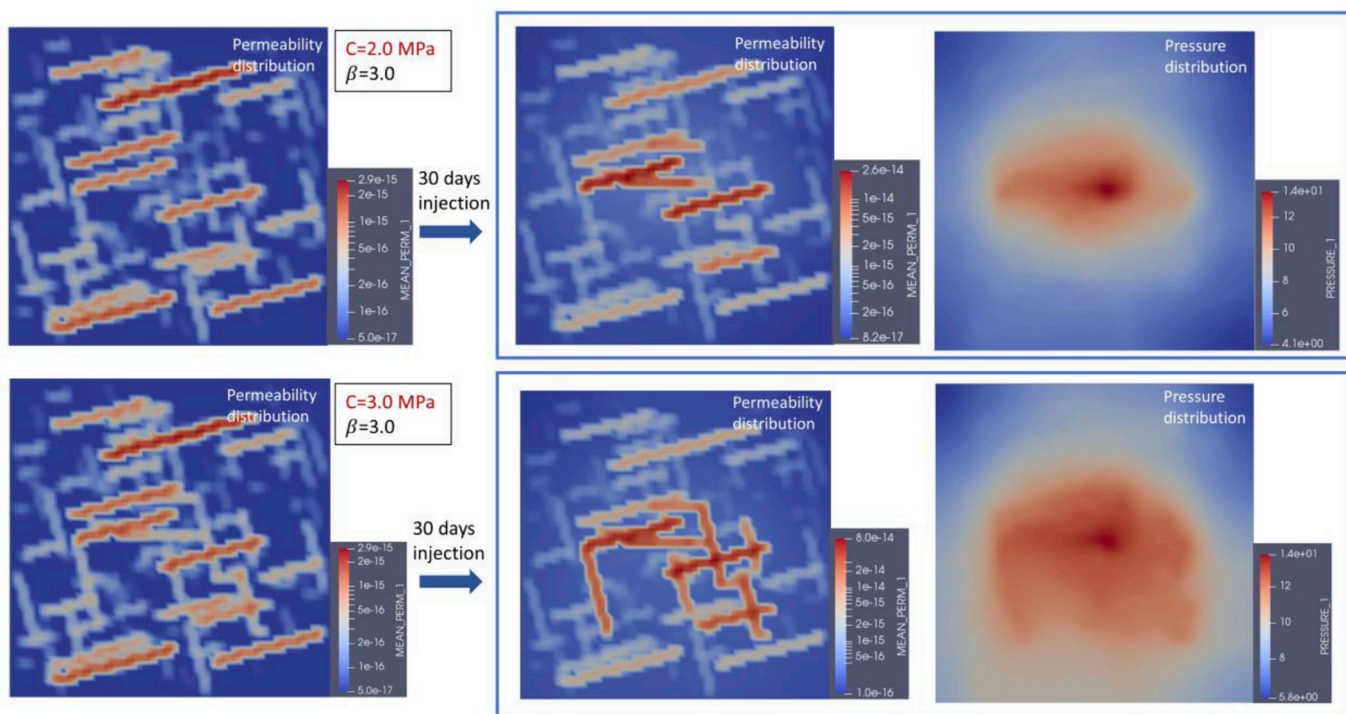
Fig. 15. Permeability and pressure distributions before and after 30-days of injection for different cohesions.
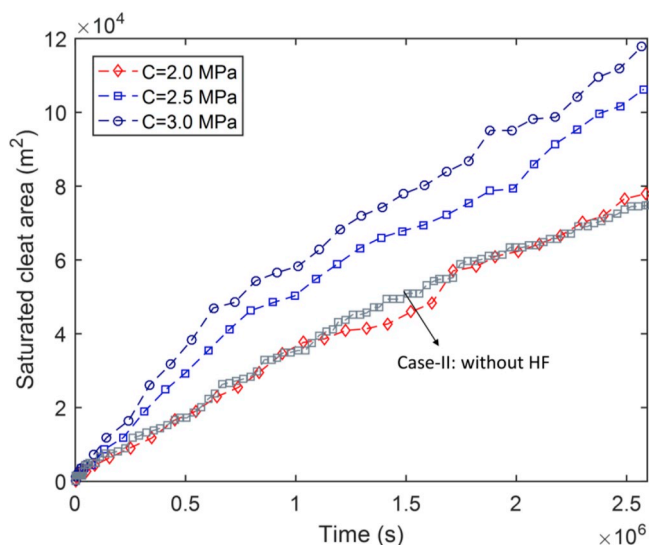

Fig. 16. Saturated cleat areas in the cases of different cohesions (proppant embedments).

only to $2.60 \times 10^{-14} \text{m}^2$ in the case of C = 2 MPa. The pressure distributions in Fig. 15 also shows that the zone of elevated pressure invades a larger area in the case of C = 3 MPa. The higher and wider pressure distribution will result in a highly permeably fracture network that comprises both dilated hydraulic- and natural-fractures. It is worth noting that some of the far-field natural fractures that are not directly connected with hydraulic fractures are also opened in the cases of a fracture wall cohesion of C = 3 MPa, as shown in Fig. 15. However, this does not occur in the case of C = 2 MPa. The saturated cleat area after 30-days of injection for different proppant embedments are shown in Fig. 16. The saturated cleat area is approximately reduced to 2/3 when cohesion is decreased by 33%, due to the influence of increased proppant embedment.

4.5. Influence of injection conditions

One potential method to enhance nutrient delivery is to increase the injection pressure and thereby the flow rate. To investigate the influence of increasing injection pressure, two more scenarios of injection at 12- and 16-MPa inlet pressure are simulated (14 MPa is the default). The evolution of fracture aperture near the inlet is examined for Case-III under these different injection pressures. At the conclusion of the injection, maximum aperture near the inlet is raised from 3.14×10^{-4} m to 3.59×10^{-4} m when the pressure increases from 12 MPa to 16 MPa. Meanwhile, the permeability reaches 7.91×10^{-14} m^2 – doubling the original magnitude. Fig. 17 shows the resultant cumulative injection volume at the three injection pressures. Once the fracture closest to the inlet is dilated, an extremely permeable pathway results. The fluid pressure quickly builds in the open fracture and then penetrates the closed fractures that are connected to it. Although the fracture system has a higher permeability at high fluid pressures, flow rate will increase slowly when the fluid pressure is close to the injection pressure. At the final stage of the injection, cumulative injection will only increase at a very slow rate. In the case of 12-MPa injection, the cumulative injected nutrient volume is 4.16×10^4 L, which is 70% of that in the case with an injection pressure of 14 MPa. Saturated surface areas (RC > 0.1) of the cases under different injection pressures are summarized in Fig. 18. A pronounced reduction in the mineral-saturated cleat area can be seen when injection pressure decreases from 16 MPa to 10 MPa in all three cases. The results demonstrate that increasing the injection pressure is a particularly effective way to enhance nutrient delivery in MECBM.

4.6. Estimation of methane yields

From the foregoing, the microbial generation of methane may be scaled to field scale using the appropriate nutrient-penetration. Biogasification progresses with a time-lag while the environment become stable after injection and metabolization ultimately evolves. Once methane generation initiates, the methane yields can be estimated as a function of time as (Saurabh and Harpalani, 2018):
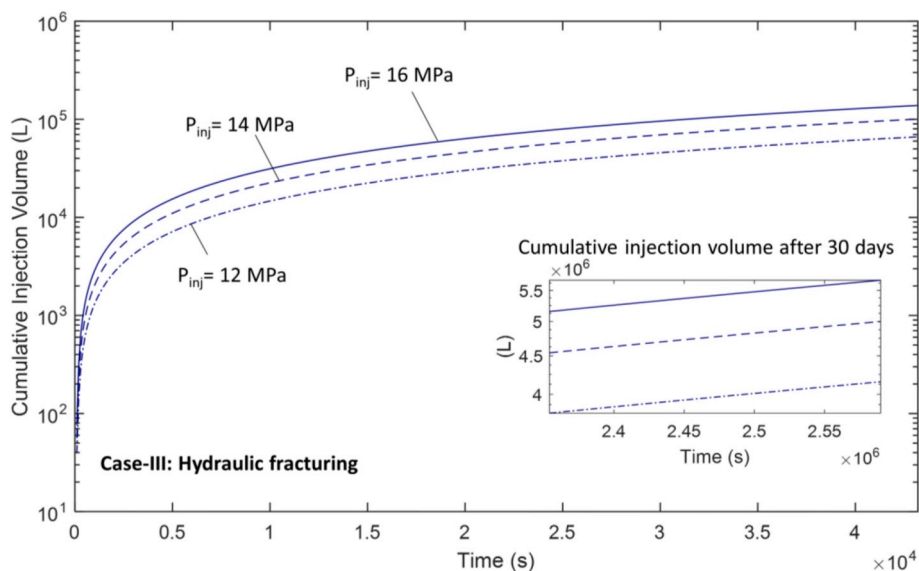
Fig. 17. Cumulative injection volume versus time at different injection pressures.

$$MY(t) = m\left[\frac{KP_0}{P_0 + (K - P_0)e^{-rt}} - P\right]_0 \quad (17)$$

where $MY(t)$ is the methane yield (mmol/g) and t is time (hours). m is a constant of proportionality (equal to unity, here). K is the carrying capacity of the environment, P_O is the initial population in the environment, r is the growth rate coefficient.

Reported rates of methane production in the laboratory bio-gasification of coal can be up to 2900 ft³/ton (4.38 mmol/g), while more moderate results show methane yields are typically in the range of 100–500 ft³/ton (0.15–0.75 mmol/g) (Bi et al., 2017; Davis et al., 2018; Green et al., 2008; Huang et al., 2013; Zhang et al., 2015, 2016a, 2016b). A few experiments also show an extremely low production <

10 ft³/ton (0.015 mmol/g) that is not considered in this study. These production differences primarily result from the selection and characteristics of supplemented amendments, temperatures, pH values, microbial compositions, and mesh sizes and ranks of coal. Methane production rates of 120.4 ft³/ton (0.17 mmol/g) reported by Green et al. (2008) and of 464.0 ft³/ton (0.7 mmol/g) reported by Bi et al. (2017) are used in this evaluation as the baseline and optimal model, respectively. Both of these used ground coal samples at 40 mesh and the influence of the large surface area of powdered coal are excluded in the calculations. As listed in Table 3 and plotted in Fig. 19, the numerical modeling results using the designed parameters effectively replicate experimental results.

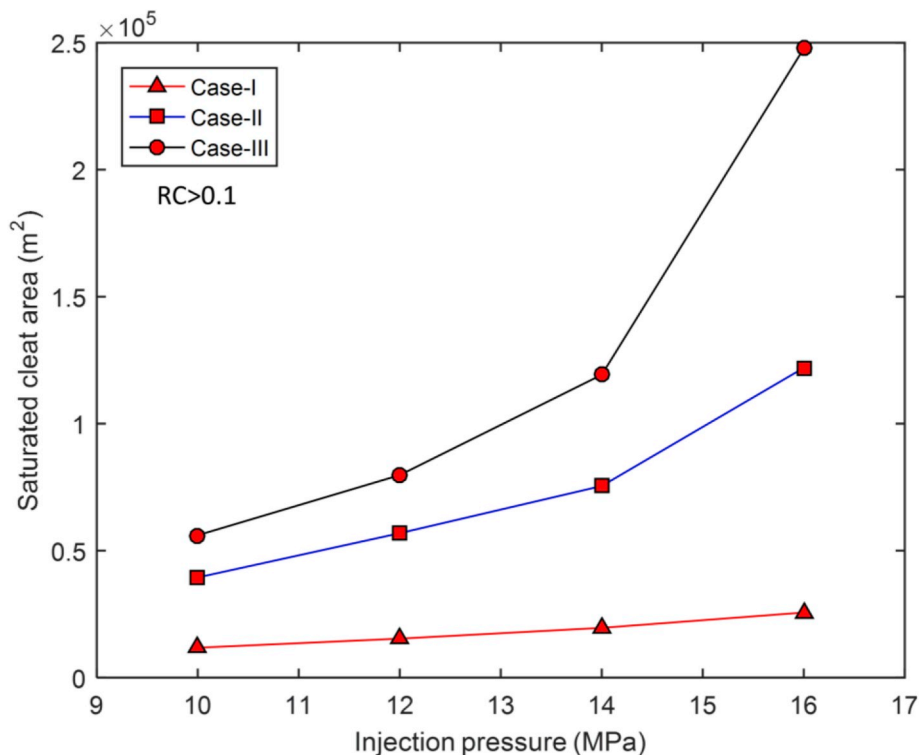The maximum production rate is only achieved in an optimal

Fig. 18. Influence of injection pressure in increasing saturated cleat area (RC > 0.1). Note that injection pressure is set constant over the first 30 days in all 12 runs.

Table 3
Modeling parameters used in the logistic equation.

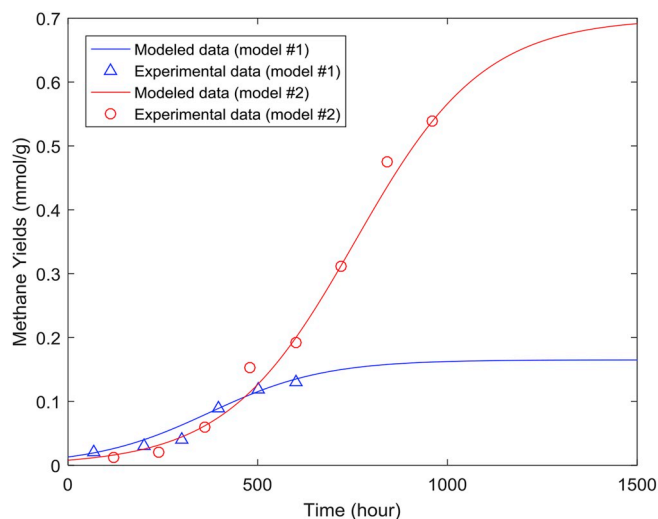|	Model#1 (Green et al., 2008)	Model#2 (Bi et al., 2017)
$P_{0\ (mmol/g)}$	0.013	0.008
K (mmol/g)	0.165	0.70
R (hr^{-1})	0.0066	0.0059

Fig. 19. Prediction of methane yields validated by reported experimental data.

environment with the added amendments at the optimal concentrations. However, a nutrient concentration gradient exists from the inlet to the far field following injection, as shown in the simulated results discussed above. For a more accurate prediction of methane yield, it is important to consider the production rate at different nutrient concentrations. To quantify the influence of concentration, an empirical equation proposed by Bi et al. (2017) is adopted in this study. Finally, the prediction equation for methane yields can be expressed as

$$MY(t) = m \left[\frac{KP_0}{P_0 + (K - P_0)e^{-rt}} - P_0 \right] \times MYR(RC) \tag{18}$$

where $MYR(RC) = -0.5504RC^2 + 1.6954RC - 0.144$. MYR is the methane yield ratio as a function of relative concentration of the nutrient components. To aid direct comparison, all the concentrations of primary components are normalized as relative concentrations. In this equation, the optimal values for ethanol, methanol, 2-propanol and sodium acetate are 27, 50, 10, and 100 mM, respectively.

The evolution of methane yields in Cases-I, −II and −III predicted via the two production models are shown in Fig. 20, where (A) and (B) are for the baseline model and the optimal model, respectively. The red-shaded zones represent the areas that have been largely saturated by nutrient and reach the maximum production rate after 60 days. The results identify that maximum methane production is in the range spanning 7.34–30.69 ft^3/ton (0.011–0.046 mmol/g) by using different stimulation methods. The reported methane production in the Illinois and the Powder River basins are ~70 ft^3/ton (Green et al., 2008; Mardon et al., 2014) – suggesting that the bio-stimulated production may reach half of its original production. Fig. 21 compares the cumulative methane yields from all scenarios. Cumulative methane yields range from 3.73×10^5 to 1.67×10^6 ft^3 in the case where nutrient transport is restricted to through the coal matrix. By using both NF network and HF stimulations, the cumulative methane yields can be boosted 4.1-fold and 5.4-fold, respectively. In the optimal scenario (Case-III + model #2 at 16-MPa injection pressure), the biogenic methane augmented over primary recovery is 1.22×10^7 ft^3, which can be produced at a rate of 200 Mcf/d for 61 days.

All prior calculations are centered around the case study in this paper. Compared to existing evaluations of MECBM recovery noted in the literature, the influences of fracture system and coal surface area are carefully considered. This paramount importance of fracture connectivity is highlighted in the production results. It can be seen that the estimated increases in methane yields are encouraging for pre-stimulation of the reservoir. However, it is still difficult to fully evaluate MECBM due to uncertainties in in-situ microbial activity and underground hydrogeologic factors. The surface area of coal available for biogasification is an important variable and is ill-constrained in CBM reservoirs. These factors must be further constrained to reduce uncertainties in the prediction of microbially-enhanced methane yields.

Although the influence of hydrofracturing in methane yields from biogasification is preliminarily analyzed, many questions remain to be answered. What fraction of coal can be ultimately converted to methane and how will this influence coal strength, porosity and permeability? How to precisely quantify the effective surface area accessible to methanogens in reservoirs? How will saturation (two-phase flow) influence the biogasification? How to better apply the coal-to-methane rate from laboratorial observation to field-scale stimulation? These are worth further investigating before microbially-enhanced CBM can be adequately utilized as a resource.

5. Conclusions

Field-scale numerical simulations of MECBM are completed using an equivalent multi-continuum method to define the effectiveness of nutrient delivery. The complex fracture pattern of natural reservoirs is represented by an overprinted discrete fracture network (DFN) to depict natural heterogeneity and anisotropy of fracture permeability in the CBM reservoir. An aperture evolution model including fracture opening, closure and propping for both natural and hydraulically-driven fracture networks is proposed to estimate permeability evolution of the DFN. A simplified PKN model is adopted to simulate fracture propagation based on the theory of linear elastic fracture mechanics (LEFM). According to the maximum circumferential normal stress criterion, a mixed mode I-II compression-shear failure criterion under high fluid pressure is used to generate wing fractures when hydraulic fractures interact with the pre-existing fracture network.

A prototypical MECBM reservoir is studied. Compared to the unstimulated and dilated cases of the natural fracture network, the hydraulically stimulated case demonstrates the effectiveness of hydraulic fracturing to enhance nutrient delivery. Cumulative injection volume and saturated cleat area are analyzed in each case. Concentration evolution patterns of all the media are compared. The results show that without a natural fracture system, the ability to deliver nutrient through the coal matrix is extremely limited. Pre-existing natural fractures oblique to the principal stress direction provide more permeable pathways for solute transport and nutrient delivery. Hydraulically stimulated fracture pathways, especially when connecting to a natural fracture network, may optimally deliver soluble nutrients to significant distances from the injection well, thereby increasing nutrient delivery and the efficiency of methane recovery. However, this behavior may be curtailed by the effects of proppant embedment. Decreasing proppant embedment and increasing injection pressure can facilitate the nutrient transport. In the optimal scenario, methane yields in the stimulated case is improved 5-fold that of the unstimulated case.

The coupled mechanical and fluid transport models used in this study have been rigorously validated and are reported elsewhere (Gan and Elsworth, 2016; Taron et al., 2009b). Here, the proposed fracture propagation model and the evolution of the aperture change for the propped fracture are examined.
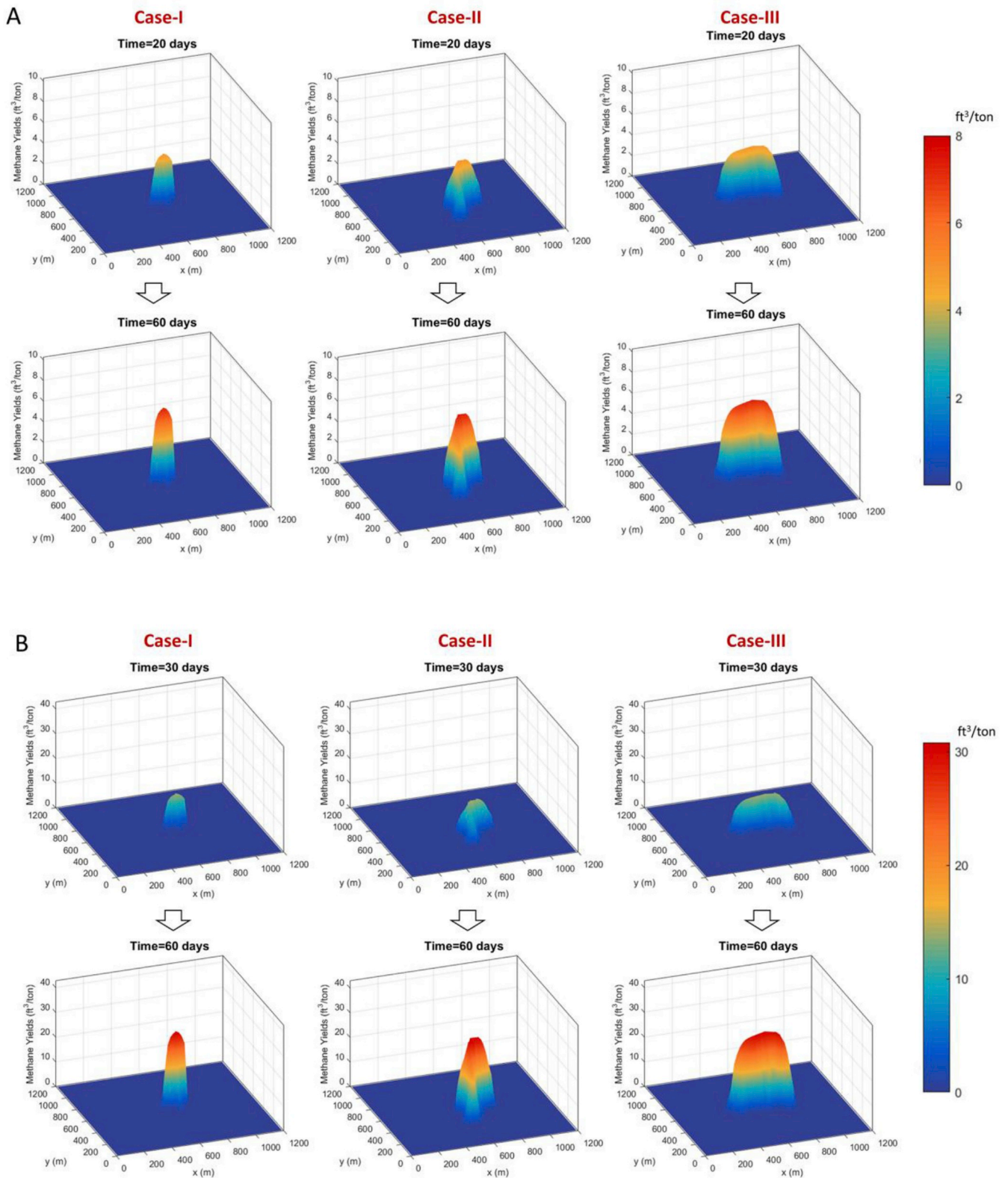
Fig. 20. Evolution of methane yields for the three cases using (A) the baseline production model and (B) the optimal production model.
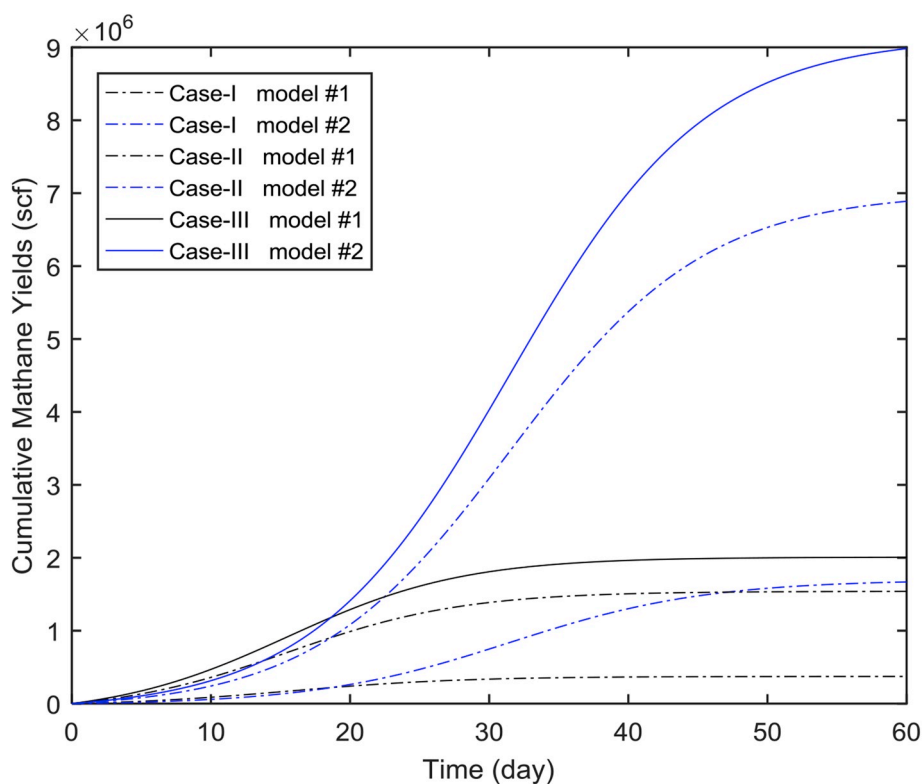
Fig. 21. Cumulative methane yields in the three cases using the baseline production model (model #1) and the optimal production model (model #2).

Acknowledgement

Appendix. Supplementary data

Supplementary data to this article can be found online at https://doi.org/10.1016/j.jngse.2018.10.012.

References

Alramahi, B., Sundberg, M.I., 2012. Proppant embedment and conductivity of hydraulic fractures in shales. Int. J. Eng. Sci. 77, 14–23. https://doi.org/10.1016/j.ijengsci.2013.12.005.

Baghbanan, A., Jing, L., 2007. Hydraulic properties of fractured rock masses with correlated fracture length and aperture. Int. J. Rock Mech. Min. Sci. 44 (5), 704–719. https://doi.org/10.1016/j.ijrmms.2006.11.001.

Bi, Z., Zhang, J., Park, S., Harpalani, S., Liang, Y., 2017. A formation water-based nutrient recipe for potentially increasing methane release from coal in situ. Fuel 209, 498–508. July. https://doi.org/10.1016/j.fuel.2017.08.008.

Biot, M.A., 1941. General theory of three-dimensional consoli- dation. J. Appl. Phys. 12 (2), 155–164.

Chin, L.Y., Raghavan, R., Thomas, L.K., 2000. Fully coupled geomechanics and fluid-flow analysis of wells with stress-dependent permeability. SPE J. 5 (01), 32–45. https://doi.org/10.2118/58968-PA.

Cokar, M., Ford, B., Kallos, M.S., Gates, I.D., 2013. New gas material balance to quantify biogenic gas generation rates from shallow organic-matter-rich shales. Fuel 104, 443–451. https://doi.org/10.1016/j.fuel.2012.06.054.

Crandall, D., Bromhal, G., Karpyn, Z.T., 2010. Numerical simulations examining the relationship between wall-roughness and fluid flow in rock fractures. Int. J. Rock Mech. Min. Sci. 47 (5), 784–796. https://doi.org/10.1016/j.ijrmms.2010.03.015.

Daneshy, a A., 2003. Off-balance Growth : a New Concept in Hydraulic Fracturing. pp. 78–85. April. https://doi.org/10.2118/80992-MS.

Davis, K.J., Lu, S., Barnhart, E.P., Parker, A.E., Fields, M.W., Gerlach, R., 2018. Type and amount of organic amendments affect enhanced biogenic methane production from coal and microbial community structure. Fuel 211, 600–608. June 2017. https://doi.org/10.1016/j.fuel.2017.09.074.

Detournay, E., Cheng, a. H.-D., McLennan, J.D., 1990. A poroelastic PKN hydraulic fracture model based on an explicit moving mesh algorithm. J. Energy Resour. Technol. 112 (4), 224. https://doi.org/10.1115/1.2905762.

Elsworth, B.D., Bai, M., 1992. Flow-deformation response of dual-porosity media. 118

(1), 107–124.

Erdogan, F., Sih, G.C., 1963. On the crack extension in plane loading and transverese shear. J. Basic Eng. 85, 519–527.

Faiz, M., Hendry, P., 2006. Significance of microbial activity in Australian coal bed methane reservoirs—a review. Bull. Can. Petrol. Geol. 54 (3), 261–272. https://doi.org/10.2113/gscpgbull.54.3.261.

Fang, Y., Elsworth, D., Cladouhos, T.T., 2015. Estimating In-situ Permeability of Stimulated EGS Reservoirs Using MEQ Moment Magnitude : an Analysis of Newberry MEQ Data, C. pp. 1–10 1965.

Fu, P., Johnson, S.M., Carrigan, C.R., 2013. An explicitly coupled hydro-geomechanical model for simulating hydraulic fracturing in arbitrary discrete fracture networks. Int. J. Numer. Anal. Method Geomech. 37 (14), 2278–2300. https://doi.org/10.1002/nag.2135.

Gan, Q., Elsworth, D., 2016. A continuum model for coupled stress and fluid flow in discrete fracture networks. Geomech. Geophys. Geo-Energy Geo-Resour. 2 (1), 43–61. https://doi.org/10.1007/s40948-015-0020-0.

Ghanbarian, B., Perfect, E., Liu, H.-H., 2018. A geometrical APERTURE–WIDTH relationship for rock fractures. Fractals 27 (1), 1940002. https://doi.org/10.1142/S0218348X19400024.

Ghassemi, a., Zhang, Q., 2006. Porothermoelastic analysis of the response of a stationary crack using the displacement discontinuity method. J. Eng. Mech. 132 (1), 26–33. https://doi.org/10.1061/(ASCE)0733-9399(2006)132:1(26).

Green, M.S., Flanegan, K.C., Gilcrease, P.C., 2008. Characterization of a methanogenic consortium enriched from a coalbed methane well in the Powder River Basin, U.S.A. Int. J. Coal Geol. 76 (1–2), 34–45. https://doi.org/10.1016/j.coal.2008.05.001.

Geertsma, J., De Klerk, F., 1969. A rapid method of predicting width and extent of hydraulically induced fractures. J. Petrol. Technol. 21, 1571–1581. https://doi.org/10.2118/2458-PA.

Green, A.E., Sneddon, I.N., 1950. The distribution of stress in the neighbourhood of a flat elliptical crack in an elastic solid. Math. Proc. Camb. Phil. Soc. 46, 159–163. https://doi.org/10.1017/S0305004100025585.

Guo, J., Wang, J., Liu, Y., Chen, Z., Zhu, H., 2017. Analytical analysis of fracture conductivity for sparse distribution of proppant packs. J. Geophys. Eng. 14 (3), 599–610. https://doi.org/10.1088/1742-2140/aa6215.

Huang, N., Jiang, Y., Liu, R., Xia, Y., 2018. Size effect on the permeability and shear induced flow anisotropy of fractal rock fractures. Fractals 26 (2), 1840001. https://doi.org/10.1142/S0218348X18400017.

Huang, S., Liu, D., Yao, Y., Gan, Q., Cai, Y., Xu, L., 2017. Natural fractures initiation and fracture type prediction in coal reservoir under different in-situ stresses during hydraulic fracturing. J. Nat. Gas Sci. Eng. 43, 69–80. https://doi.org/10.1016/j.jngse.2017.03.022.

Huang, Z., Urynowicz, M.A., Colberg, P.J.S., 2013. Stimulation of biogenic methane generation in coal samples following chemical treatment with potassium permanganate. Fuel 111, 813–819. https://doi.org/10.1016/j.fuel.2013.03.079.

Jamari, J., Schipper, D.J., 2006. Experimental investigation of fully plastic contact of a sphere against a hard flat. J. Tribol. 128 (2), 230. https://doi.org/10.1115/1.

2164470.

Jones, E.J.P., Voytek, M. a., Corum, M.D., Orem, W.H., 2010. Stimulation of methane generation from nonproductive coal by addition of nutrients or a microbial consortium. Appl. Environ. Microbiol. 76 (21), 7013–7022. https://doi.org/10.1128/AEM.00728-10.

Kirk, M.F., Martini, A.M., Breecker, D.O., Colman, D.R., Takacs-Vesbach, C., Petsch, S.T., 2012. Impact of commercial natural gas production on geochemistry and microbiology in a shale-gas reservoir. Chem. Geol. 332–333, 15–25. https://doi.org/10.1016/j.chemgeo.2012.08.032.

Kumar, H., Elsworth, D., Liu, J., Pone, D., Mathews, J.P., 2015. Permeability evolution of propped artificial fractures in coal on injection of CO2. J. Petrol. Sci. Eng. 133, 695–704. https://doi.org/10.1016/j.petrol.2015.07.008.

Lacy, L.L., Rickards, A.R., Bilden, D.M., 1998. Fracture width and embedment testing in soft reservoir sandstone. SPE Drill. Complet. 13 (1), 25–29. https://doi.org/10.2118/36421-PA.

Lee, D.S., Elsworth, D., Yasuhara, H., Weaver, J.D., Rickman, R., 2010. Experiment and modeling to evaluate the effects of proppant-pack diagenesis on fracture treatments. J. Petrol. Sci. Eng. 74 (1–2), 67–76. https://doi.org/10.1016/j.petrol.2010.08.007.

Li, K., Gao, Y., Lyu, Y., Wang, M., 2015. New mathematical models for calculating proppant embedment and fracture conductivity. SPE J. 20 (03), 496–507. https://doi.org/10.2118/155954-PA.

Liu, C., Zachara, J.M., Qafoku, N.P., Wang, Z., 2008. Scale-dependent desorption of uranium from contaminated subsurface sediments. Water Resour. Res. 44 (8), 1–13. https://doi.org/10.1029/2007WR006478.

Liu, J., Chen, Z., Elsworth, D., Miao, X., Mao, X., 2011. Evolution of coal permeability from stress-controlled to displacement-controlled swelling conditions. Fuel 90 (10), 2987–2997. https://doi.org/10.1016/j.fuel.2011.04.032.

Liu, R., Jiang, Y., Huang, N., Sugimoto, S., 2018. Hydraulic properties of 3D crossed rock fractures by considering anisotropic aperture distributions. Adv. Geo-Energy Res. 2 (2), 113–121. https://doi.org/10.26804/ager.2018.02.01.

Liu, T., Cao, P., Lin, H., 2014a. Damage and fracture evolution of hydraulic fracturing in compression-shear rock cracks. Theor. Appl. Fract. Mech. 74 (1), 55–63. https://doi.org/10.1016/j.tafmec.2014.06.013.

Liu, Z., Chen, M., Zhang, G., 2014b. Analysis of the influence of a natural fracture network on hydraulic fracture propagation in carbonate formations. Rock Mech. Rock Eng. 47 (2), 575–587. https://doi.org/10.1007/s00603-013-0414-7.

Lloyd, K., 2015. Beyond known methanogens. Science 350 (6259), 384. https://doi.org/10.1126/science.aad4066.

Long, J.C.S., Witherspoon, P. a., 1985. The relationship of the degree of interconnection to permeability in fracture networks. J. Geophys. Res. 90 (B4), 3087. https://doi.org/10.1029/JB090iB04p03087.

Mardon, S.M., Eble, C.F., Hower, J.C., Takacs, K., Mastalerz, M., Marc Bustin, R., 2014. Organic petrology, geochemistry, gas content and gas composition of Middle Pennsylvanian age coal beds in the Eastern Interior (Illinois) Basin: implications for CBM development and carbon sequestration. Int. J. Coal Geol. 127, 56–74. https://doi.org/10.1016/j.coal.2014.02.002.

McClure, M., Horne, R.N., 2013. Discrete Fracture Network Modeling of Hydraulic Stimulation: Coupling Flow and Geomechanics. Springer, Berlin.

McGuire, T.P., Elsworth, D., Karcz, Z., 2013. Experimental measurements of stress and chemical controls on the evolution of fracture permeability. Transport Porous Media 98 (1), 15–34. https://doi.org/10.1007/s11242-013-0123-4.

Min, K.B., Jing, L., 2003. Numerical determination of the equivalent elastic compliance tensor for fractured rock masses using the distinct element method. Int. J. Rock Mech. Min. Sci. 40 (6), 795–816. https://doi.org/10.1016/S1365-1609(03)00038-8.

Moore, T.A., 2012. Coalbed methane: a review. Int. J. Coal Geol. 101, 36–81. https://doi.org/10.1016/j.coal.2012.05.011.

Noiriel, C., Renard, F., Doan, M.L., Gratier, J.P., 2010. Intense fracturing and fracture sealing induced by mineral growth in porous rocks. Chem. Geol. 269 (3–4), 197–209. https://doi.org/10.1016/j.chemgeo.2009.09.018.

Nordgren, R.P., 1972. Propagation of a vertical hydraulic fracture. Soc. Petrol. Eng. J. 12 (04), 306–314. https://doi.org/10.2118/3009-PA.

Oda, M., 1986. An equivalent continuum model for coupled stress and fluid flow analysis in jointed rock masses. Water Resour. Res. 22 (13), 1845–1856. https://doi.org/10.1029/WR022i013p01845.

Olson, J.E., 2003. Sublinear scaling of fracture aperture versus length: an exception or the rule? J. Geophys. Res.: Solid Earth 108 (B9). https://doi.org/10.1029/2001JB000419.

Palmer, I., 2010. Coalbed methane completions: a world view. Int. J. Coal Geol. 82 (3–4), 184–195. https://doi.org/10.1016/j.coal.2009.12.010.

Park, S.Y., Liang, Y., 2016. Biogenic methane production from coal: a review on recent research and development on microbially enhanced coalbed methane (MECBM). Fuel 166, 258–267. https://doi.org/10.1016/j.fuel.2015.10.121.

Ritter, D., Vinson, D., Barnhart, E., Akob, D.M., Fields, M.W., Cunningham, A.B., McIntosh, J.C., 2015. Enhanced microbial coalbed methane generation: a review of research, commercial activity, and remaining challenges. Int. J. Coal Geol. 146, 28–41. https://doi.org/10.1016/j.coal.2015.04.013.

Rutqvist, J., Leung, C., Hoch, A., Wang, Y., Wang, Z., 2013. Journal of Rock Mechanics and Geotechnical Engineering Linked multicontinuum and crack tensor approach for modeling of coupled geomechanics, fluid flow and transport in fractured rock. Integr. Med. Res. 5 (1), 18–31. https://doi.org/10.1016/j.jrmge.2012.08.001.

Rutqvist, J., Stephansson, O., 2003. The role of hydromechanical coupling in fractured rock engineering. Hydrogeol. J. 11 (1), 7–40. https://doi.org/10.1007/s10040-002-0241-5.

Sammis, C.G., Ashby, M.F., 1986. The failure of brittle porous solids under compressive

stress states. Acta Metall. 34 (3), 511–526. https://doi.org/10.1016/0001-6160(86)90087-8.

Saurabh, S., Harpalani, S., 2018. Modeling of microbial methane generation from coal and assessment of its impact on flow behavior. Fuel 216 (November 2017), 274–283. https://doi.org/10.1016/j.fuel.2017.12.015.

Scott, A., 1999. Improving coal gas recovery with microbially enhanced coalbed methane. In: Coalbed Methane: Scientific, Environmental and …, 89–110, . https://doi.org/10.1007/978-94-017-1062-6_7.

Seidle, J.R., Huitt, L.G., 1995. Experimental measurement of coal matrix shrinkage due to gas desorption and implications for cleat permeability increases. In: International Meeting on Petroleum Engineering, . https://doi.org/10.2118/30010-MS.

Stephansson, S., David, M.-T., 2004. Investigating how proppant packs change under stress. In: Proceedings of SPE Annual Technical Conference and Exhibition, . https://doi.org/10.2523/90562-MS.

Stolper, D.A., Lawson, M., Davis, C.L., Ferreira, A.A., Santos Neto, E.V., Ellis, G.S., Eiler, J.M., 2014. Formation temperatures of thermogenic and biogenic methane. Science 344 (6191), 1500–1503. https://doi.org/10.1126/science.1254509.

Strąpoć, D., Mastalerz, M., Dawson, K., Macalady, J., Callaghan, A.V., Wawrik, B., Ashby, M., 2011. Biogeochemistry of microbial coal-bed methane. Annu. Rev. Earth Planet Sci. 39 (1), 617–656. https://doi.org/10.1146/annurev-earth-040610-133343.

Taron, J., Elsworth, D., 2010. Coupled mechanical and chemical processes in engineered geothermal reservoirs with dynamic permeability. Int. J. Rock Mech. Min. Sci. 47 (8), 1339–1348. https://doi.org/10.1016/j.ijrmms.2010.08.021.

Taron, J., Elsworth, D., Min, K.B., 2009a. Numerical simulation of thermal-hydrologic-mechanical-chemical processes in deformable, fractured porous media. Int. J. Rock Mech. Min. Sci. 46 (5), 842–854. https://doi.org/10.1016/j.ijrmms.2009.01.008.

Taron, J., Elsworth, D., Min, K.B., 2009b. Numerical simulation of thermal-hydrologic-mechanical-chemical processes in deformable, fractured porous media. Int. J. Rock Mech. Min. Sci. 46 (5), 842–854. https://doi.org/10.1016/j.ijrmms.2009.01.008.

Ulrich, G., Bower, S., 2008. Active methanogenesis and acetate utilization in Powder River Basin coals, United States. Int. J. Coal Geol. 76 (1–2), 25–33. https://doi.org/10.1016/j.coal.2008.03.006.

Volk, L., Raible, C., Carroll, H., Spears, J., 1981. Embedment of high strength proppant into low-permeability reservoir rock. In: Proceedings of SPE/DOE Low Permeability Gas Reservoirs Symposium, . https://doi.org/10.2118/9867-MS.

Wang, J., Elsworth, D., Denison, M.K., 2018a. Hydraulic fracturing with leakoff in a pressure-sensitive dual porosity medium. Int. J. Rock Mech. Min. Sci. 107, 55–68. April. https://doi.org/10.1016/j.ijrmms.2018.04.042.

Wang, J., Elsworth, D., Wu, Y., Liu, J., Zhu, W., Liu, Y., 2018b. The influence of fracturing fluids on fracturing processes: a comparison between water, oil and SC-CO2. Rock Mech. Rock Eng. 51 (1), 299–313. https://doi.org/10.1007/s00603-017-1326-8.

Wang, S., Elsworth, D., Liu, J., 2012. A mechanistic model for permeability evolution in fractured sorbing media. J. Geophys. Res.: Solid Earth 117, 1–17. September 2011. https://doi.org/10.1029/2011JB008855.

Wang, S., Elsworth, D., Liu, J., 2013. Permeability evolution during progressive deformation of intact coal and implications for instability in underground coal seams. Int. J. Rock Mech. Min. Sci. 58, 34–45. https://doi.org/10.1016/j.ijrmms.2012.09.005.

Wen, Q., Zhang, S., Wang, L., Liu, Y., Li, X., 2007. The effect of proppant embedment upon the long-term conductivity of fractures. J. Petrol. Sci. Eng. 55 (3–4), 221–227. https://doi.org/10.1016/j.petrol.2006.08.010.

Wu, Y., Liu, J., Chen, Z., Elsworth, D., Pone, D., 2011. A dual poroelastic model for CO2-enhanced coalbed methane recovery. Int. J. Coal Geol. 86, 177–189. https://doi.org/10.1016/j.coal.2011.01.004.

Zhang, J., Kamenov, A., Zhu, D., Hill, D., 2013. Laboratory measurement of hydraulic fracture conductivities in the Barnett shale. In: International Petroleum Technology Conference, pp. 1–12. https://doi.org/10.2523/16444-MS.

Zhang, J., Liang, Y., Harpalani, S., 2016a. Optimization of methane production from bituminous coal through biogasification. Appl. Energy 183, 31–42. https://doi.org/10.1016/j.apenergy.2016.08.153.

Zhang, J., Liang, Y., Pandey, R., Harpalani, S., 2015. Characterizing microbial communities dedicated for conversion of coal to methane in situ and ex situ. Int. J. Coal Geol. 146, 145–154. https://doi.org/10.1016/j.coal.2015.05.001.

Zhang, J., Park, S.Y., Liang, Y., Harpalani, S., 2016b. Finding cost-effective nutrient solutions and evaluating environmental conditions for biogasifying bituminous coal to methane ex situ. Appl. Energy 165, 559–568. https://doi.org/10.1016/j.apenergy.2015.12.067.

Zhang, X., Jeffrey, R.G., 2014. Role of overpressurized fluid and fluid-driven fractures in forming fracture networks. J. Geochem. Explor. 144 (PA), 194–207. https://doi.org/10.1016/j.gexplo.2014.03.021.

Zhao, Y., Gong, S., Zhang, C., Zhang, Z., Jiang, Y., 2018. Fractal characteristics of crack propagation in coal under impact loading. Fractals 26 (02), 1840014. https://doi.org/10.1142/S0218348X18400145.

Zhao, Z., Jing, L., Neretnieks, I., 2010. Evaluation of hydrodynamic dispersion parameters in fractured rocks. J. Rock Mech. Geotech. Eng. 2 (3), 243–254. https://doi.org/10.3724/SP.J.1235.2010.00243.

Zhi, S., Elsworth, D., 2016. The role of gas desorption on gas outbursts in underground mining of coal. Geomech. Geophy. Geo-Energy Geo-Resour. 2 (3), 151–171. https://doi.org/10.1007/s40948-016-0026-2.

Zou, M., Wei, C., Zhang, M., Shen, J., Chen, Y., Qi, Y., 2013. Classifying coal pores and estimating reservoir parameters by nuclear magnetic resonance and mercury intrusion porosimetry. Energy Fuels 27 (7), 3699–3708. https://doi.org/10.1021/ef400421u.